



IIMPI
INSTITUTO DE
INGENIERIA MECANICA
Y PRODUCCION INDUSTRIAL



UNIVERSIDAD
DE LA REPUBLICA
URUGUAY

Evaluation of Concentrating Solar Power technologies for their application in Uruguay

Agustín Ghazarian Hagopian

Programa de Posgrado en Ingeniería de la Energía
Facultad de Ingeniería
Universidad de la República

Montevideo – Uruguay
Junio de 2021



IIMPI
INSTITUTO DE
INGENIERIA MECANICA
Y PRODUCCION INDUSTRIAL



UNIVERSIDAD
DE LA REPUBLICA
URUGUAY

Evaluation of Concentrating Solar Power technologies for their application in Uruguay

Agustín Ghazarian Hagopian

Tesis de Maestría presentada al Programa de Posgrado en Ingeniería de la Energía, Facultad de Ingeniería de la Universidad de la República, como parte de los requisitos necesarios para la obtención del título de Magíster en Ingeniería de la Energía.

Director:

Dr.Ing. Pedro Galione

Codirector:

Dr.Ing. Pedro Curto

Director académico:

Dr.Ing. Pedro Galione

Montevideo – Uruguay

Junio de 2021

Ghazarian Hagopian, Agustín

Evaluation of Concentrating Solar Power technologies for their application in Uruguay / Agustín Ghazarian Hagopian. - Montevideo: Universidad de la República, Facultad de Ingeniería, 2021.

XVII, 96 p.: il.; 29, 7cm.

Director:

Pedro Galione

Codirector:

Pedro Curto

Director académico:

Pedro Galione

Tesis de Maestría – Universidad de la República, Programa en Ingeniería de la Energía, 2021.

Referencias bibliográficas: p. 69 – 73.

1. Concentración solar,
2. Energía Solar,
3. Optimización LCOE. I. Galione, Pedro, *et al.* II. Universidad de la República, Programa de Posgrado en Ingeniería de la Energía. III. Título.

INTEGRANTES DEL TRIBUNAL DE DEFENSA DE TESIS

D.Sc. Prof. Nombre del 1er Examinador Apellido

Ph.D. Prof. Nombre del 2do Examinador Apellido

D.Sc. Prof. Nombre del 3er Examinador Apellido

Ph.D. Prof. Nombre del 4to Examinador Apellido

Ph.D. Prof. Nombre del 5to Examinador Apellido

Montevideo – Uruguay

Junio de 2021

Agradecimientos

En primer lugar quisiera agradecer a mis tutores Pedro Galione y Pedro Curto por su tiempo, guía y sugerencias que fueron clave en el desarrollo de este trabajo. En segundo lugar a la ANII por el apoyo económico y por último a todos quienes, de alguna forma u otra, me acompañaron en este proceso.

Here comes the sun

George Harrison

RESUMEN

Las tecnologías de concentración solar (por sus siglas en inglés, CSP) están ganando interés a nivel mundial ya que constituyen una alternativa renovable para la generación de energía eléctrica, que a diferencia de la tecnologías eólicas y fotovoltaicas, puede fácilmente incorporar almacenamiento de energía. Este trabajo estudia la viabilidad de incorporar en Uruguay plantas del tipo Torre Central y Cilindro Parabólico. Se implementa un código propio en OCTAVE, el cual es validado contra un software preexistente y un estudio realizado previamente para Uruguay. Una extensa revisión bibliográfica es presentada para determinar los costos de inversión inicial, operación y mantenimiento e impuestos. Considerando estos costos se optimiza tanto el campo solar como el almacenamiento térmico mediante la búsqueda del mínimo costo nivelado de la electricidad (LCOE) para 5 ubicaciones diferentes en donde se cuenta con años meteorológicos típicos. Para los casos óptimos, se presenta el LCOE junto con varios resultados energéticos como electricidad generada y pérdidas.

Palabras claves:

Concentración solar, Energía Solar, Optimización LCOE.

ABSTRACT

Concentrating Solar Power (CSP) technologies are getting increasing attention from researchers all around the world, since they represent a renewable alternative for power generation that, unlike wind and photovoltaic technologies, can easily incorporate thermal storage. The current work present a viability study for the two main CSP technologies implemented around the world, Solar Power Tower (SPT) and Parabolic Trough (PT). An own code implemented in OCTAVE is developed and validated against available software and a previous work for Uruguay study case. An extensive literature review is presented in order to evaluate the initial investment costs, operation and maintainance costs and taxes that should be considered. Considering these costs, the solar field and storage sizes are optimized in order to minimize the levelized cost of energy (LCOE) for 5 different locations, where typical meteorological years are available. For the optimum cases, LCOE is calculated along with many energy results such as generated electricity and energy losses. Keywords:

Concentrating Solar Power, Solar Energy, LCOE Optimization.

List of Figures

1.1	CSP plants components [1].	2
1.2	Parabolic Trough collector [2].	3
1.3	Parabolic Trough plant scheme [3].	3
1.4	Solar Power Tower plant [4].	4
1.5	Solar Power Tower plant [5].	4
1.6	Parabolic dish technology [6].	5
1.7	Fresnel technology [1].	6
1.8	Fresnel plant loop [7].	6
1.9	CSP Global installed capacity evolution [9].	7
1.10	Installed CSP technologies and their market share, in 2018. [1].	8
1.11	Levelized cost of energy in different locations [9].	8
1.12	CSP capacity factor and electricity cost [10]	10
1.13	Renewable electricity price comparison [10]	10
1.14	Uruguayan primary energy consumption [11].	11
1.15	Hydropower generation different years [12].	12
1.16	Electricity demand evolution in Uruguay, own elaboration from data obtained in [11].	13
1.17	Annual average daily horizontal irradiation map [8].	14
2.1	Shadowing between structures [3].	19
2.2	Heat flows in Parabolic Trough collectors [3].	20
2.3	Resistance diagram, own elaboration.	21
2.4	Solar field algorithm scheme, own elaboration.	27
2.5	Typical generation plant power block. T_A and T_B are the high and low pressure turbine stages respectively, C the condenser, PA the water pre-heater, Des the deaerator and GV the steam generator, own elaboration.	28
2.6	Power block efficiency [23]	31

2.7	HTF-steam heat exchanger, own elaboration	33
2.8	Salt mass flow calculation algorithm, own elaboration.	34
2.9	Flow configuration, own elaboration.	36
2.10	Flow configuration when charging storage system, own elaboration.	37
2.11	Flow configuration when discharging storage system, own elaboration.	37
2.12	Complete solving algorithm, own elaboration	38
2.13	Energy balance to receiver [5].	40
2.14	Resistance network SAM [3].	41
3.1	Solar power tower SAM vs Solida predictions	48
3.2	Parabolic trough SAM and own code vs Solida predictions	49
3.3	Initial Investment Costs Figure obtained from [30] modified to show this work prediction in black (year 2020)	51
4.1	LCOE optimization Power Tower Salto study case, heliostat area $66.1m^2$. Own elaboration utilizing SAM.	54
4.2	LCOE optimization Parabolic Trough Salto study case, loop area $3462m^2$. Own elaboration utilizing SAM.	54
4.3	Levelized cost of energy in different locations including obtained results for both scenarios (SPT in blue, PT in red), modified from [9].	56
4.4	Salto January and July mean DNI, own elaboration utilizing SAM.	59
4.5	SPT mean January and July generation for Salto optimal study case, own elaboration utilizing SAM.	59
4.6	PT mean January and July generation for Salto optimal study case, own elaboration utilizing SAM.	60
4.7	SPT monthly generation prediction for Salto optimal study case, own elaboration utilizing SAM.	60
4.8	PT monthly generation prediction for Salto optimal study case, own elaboration utilizing SAM.	61
4.9	SPT losses for Salto optimal study case, own elaboration utilizing [32].	62
4.10	PT losses for Salto optimal study case, own elaboration utilizing [32].	62

4.11	SPT optical efficiency Salto study case, own elaboration utilizing SAM.	63
4.12	PT optical efficiency Salto study case, own elaboration utilizing SAM.	64
4.13	Cosine effect. Source [5].	64
4.14	Noon summer (black heliostats) and winter (sky blue heliostats) configuration , own elaboration utilizing [33].	65
4.15	Noon summer and sun location , own elaboration using sketchup.	66
4.16	Annual energy generated as function of the available irradiance, own elaboration utilizing SAM.	66
A.1	LCOE optimization Power Tower Salto study case.	76
A.2	LCOE optimization Parabolic Trough Salto study case.	77
A.3	LCOE optimization Power Tower Colonia study case.	79
A.4	LCOE optimization Parabolic Trough Colonia study case.	80
A.5	LCOE optimization Power Tower Montevideo study case.	82
A.6	LCOE optimization Parabolic Trough Montevideo study case.	83
A.7	LCOE optimization Solar Power Tower Rivera study case.	85
A.8	LCOE optimization Parabolic Trough Rivera study case.	86
A.9	LCOE optimization Solar Power Tower Rocha study case.	88
A.10	LCOE optimization Parabolic Trough Rocha study case.	89

List of Tables

1.1	Investment cost and capacity factor of CSP technology in different locations [9].	9
1.2	Electricity source, [11].	11
1.3	Annual irradiation, mean temperature and wind speed for different locations. Data obtained from [13]	13
2.1	Air properties [22]	22
2.2	C and m constants for determining Nusselt coefficient as function of Reynolds number [22].	23
2.3	n constant for determining Nusselt coefficient as function of Prandtl number [22].	23
2.4	Weighting factors [28].	43
3.1	System Advisor Model Validation, own elaboration.	47
3.2	System Advisor model and own code validation against Solida [18], own elaboration.	48
3.3	Decentralization punctuation [28].	52
3.4	Final tax exoneration.	52
4.1	Solar Power Tower optimal configuration and LCOE, own elaboration utilizing SAM.	55
4.2	Parabolic Trough optimal configuration and LCOE, own elaboration utilizing SAM.	55
4.3	LCOE calculation considering favorable investment conditions for Salto.	55
4.4	LCOE ($\frac{USD}{MWh}$) comparison salto study-case. Adapted LCOE considers electricity generation degradation and inflationary effects	57

4.5	LCOE sensitivity for Salto optimal study case, own elaboration utilizing SAM.	57
4.6	Annual electricity generation, own elaboration utilizing SAM.	58
4.7	Location effect, own elaboration utilizing SAM.	66
A.1	Solar Power Tower optimal configuration Salto.	75
A.2	Parabolic Trough optimal configuration Salto.	76
A.3	Main results for optimal SPT plant located in Salto.	78
A.4	Main results for optimal PT plant located in Salto.	78
A.5	Solar Power Tower optimal configuration Colonia.	79
A.6	Parabolic Trough optimal configuration Colonia.	80
A.7	Main results for optimal SPT plant located in Colonia.	81
A.8	Main results for optimal PT plant located in Colonia.	81
A.9	Solar Power Tower optimal configuration Montevideo.	82
A.10	Parabolic Trough optimal configuration Montevideo.	83
A.11	Main results for optimal SPT plant located in Montevideo.	84
A.12	Main results for optimal PT plant located in Montevideo	84
A.13	Solar Power Tower optimal configuration Rivera.	85
A.14	Parabolic Trough optimal configuration Rivera.	86
A.15	Main results for optimal SPT plant located in Rivera.	87
A.16	Main results for optimal PT plant located in Rivera.	87
A.17	Solar Power Tower optimal configuration Rocha.	88
A.18	Parabolic Trough optimal configuration Rocha.	89
A.19	Main results for optimal SPT plant located in Rocha.	90
A.20	Main results for optimal PT plant located in Rocha.	91
B.1	Solar Power Tower 50 MW initial investment(I.I.) costs.	92
B.2	Solar Power Tower 100 MW initial investment (I.I.) costs.	93
B.3	Solar Power Tower unknown capacity initial investment (I.I.) costs.	93
B.4	Parabolic Trough 50MW initial investment (I.I.) cost.	93
B.5	Parabolic Trough 100MW initial investment (I.I.) cost.	94
B.6	Parabolic Trough unknown capacity initial investment (I.I.) costs.	94
B.7	USA CSP power plants initial investment [40]	94
B.8	Spain CSP power plants initial investment. Source: https://solarpaces.nrel.gov/by-country/ES	94
B.9	Specific investment costs Solar Power Tower [25].	95

B.10 Specific investment costs Parabolic Trough [25]. 95

Contents

List of Figures	ix
List of Tables	xii
1 Introduction	1
1.1 Objectives	1
1.2 Overview of different CSP technologies	1
1.2.1 Parabolic Trough	2
1.2.2 Solar power tower	3
1.2.3 Other technologies	5
1.3 Market share	7
1.4 Electric sector in Uruguay	11
1.5 Solar Resource	13
1.6 Previous works and software for CSP simulation	14
2 Methodology	16
2.1 Parabolic trough physical modeling	16
2.1.1 Solar processor	16
2.1.2 Absorber tube modeling	19
2.1.3 Solar field solver algorithm	26
2.1.4 Power cycle implementation	27
2.1.5 Heat exchanger	30
2.1.6 Storage	33
2.1.7 System operation	35
2.1.8 Whole plant algorithm	38
2.2 System Advisor Model	39
2.2.1 Solar Power Tower Model	39
2.2.2 Parabolic Trough Model	40

2.3	Economic Analysis Procedure	41
2.3.1	LCOE definition	41
2.3.2	Tax evaluation	42
2.3.3	Procedure	43
3	Parameters setting, validation and costs estimation	44
3.1	Simulation implementation	44
3.1.1	Parabolic trough	44
3.1.2	Solar Power Tower	46
3.2	Validation	47
3.2.1	Solar Power tower	47
3.2.2	Parabolic Trough	47
3.3	Costs	49
3.3.1	Initial Investment	49
3.3.2	Operation and maintainance	50
3.3.3	Taxes	51
4	Optimization and results	53
4.1	Optimization	53
4.2	Comparison against results obtained by SOLIDA	56
4.3	Sensitivity	57
4.4	Energy	58
5	Conclusions	67
	Bibliography	69
	Appendices	74
	Appendix A Results.	75
	A.1 Location: Salto	75
	A.1.1 Optimal configuration	75
	A.1.2 Energy simulation	78
	A.2 Location: Colonia	79
	A.2.1 Optimal configuration	79
	A.2.2 Energy simulation	81
	A.3 Location: Montevideo	82
	A.3.1 Optimal configuration	82

A.3.2	Energy simulation	84
A.4	Location: Rivera	85
A.4.1	Optimal configuration	85
A.4.2	Energy simulation	87
A.5	Location: Rocha	88
A.5.1	Optimal configuration	88
A.5.2	Energy simulation	90
Appendix B	Cost estimation	92

Chapter 1

Introduction

1.1 Objectives

The main objective of this thesis is to evaluate the feasibility of including Concentrating Solar Power (CSP) technologies in the Uruguayan electricity matrix. Firstly a Solar Power Tower (SPT) and Parabolic Trough (PT) solar field and storage size optimization by the minimization of the Levelized Cost of Energy (LCOE) is performed for five different locations. Considering the optimal configurations, the viability of an electricity generation plant is analyzed by its LCOE. This parameter estimates the cost of the electricity generation per generated energy unit, during the plant lifetime. A low LCOE means that the project costs are small, making the technology competitive. Energetic results for the optimal configurations are also presented and studied.

Another objective is to develop and validate an own code that simulates the Parabolic Trough technology in order to generate a better understanding of the phenomenons involved and their impact in the final result.

1.2 Overview of different CSP technologies

CSP technologies are based on the utilization of reflective surfaces to focus the solar energy in either line (Parabolic Trough and Fresnel) or point (Power Tower and Solar Parabolic Dish) collectors. The absorbed energy heats a thermal fluid (HTF) which is used to generate super-heated steam that is finally expanded in a turbine, commonly considering a Rankine cycle. The

plants are basically composed by a solar field, thermal storage and a power block (see Figure 1.1).

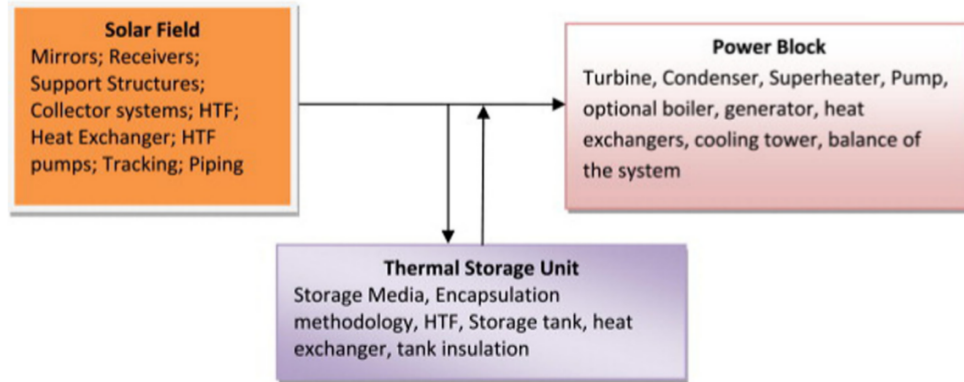


Figure 1.1: CSP plants components [1].

1.2.1 Parabolic Trough

The Parabolic Trough technology consists in large curved mirrors that reflect the solar radiation to a receiver attached to the structure (see Figure 1.2). The solar field is composed by several collectors, where axis are generally oriented in a north-south direction, allowing a east-west tracking. A heat transfer fluid (generally synthetic oil) circulates within the receiver. The employed fluid (that can reach temperatures of about $400^{\circ}C$) is then directed to a heat exchanger where super-heated steam is generated. Finally the steam is expanded in a turbine attached to a generator to produce electric power (see Fig 1.3). At good irradiance conditions, the absorbed heat is employed not only to generate steam but also to storage heat (generally by heating molten salt), to be used afterwards to generate steam, when the irradiance conditions are not favorable.



Figure 1.2: Parabolic Trough collector [2].

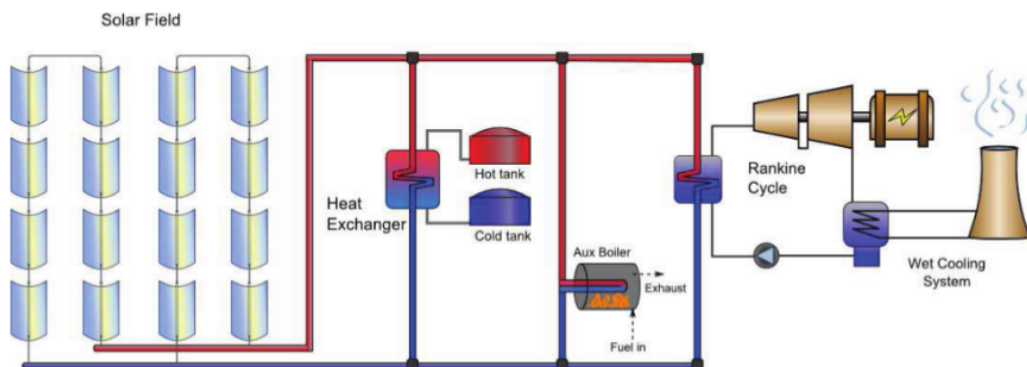


Figure 1.3: Parabolic Trough plant scheme [3].

1.2.2 Solar power tower

Unlike PT, Solar Power Tower employs mirrors to reflect sunlight to a receiver situated on top of a tower placed in the middle of the solar field (see Figure 1.4). In the receiver a working fluid (water/steam, molten salts, liquid sodium or air) is heated. In the current work, molten salt is considered as working fluid. This technology allows to reach temperatures up to 560°C (higher values than PT). It is usual that the heat transfer fluid is also employed as storage fluid. After being heated the fluid is directed to a hot tank where it is either stored or pumped into a heat exchanger to produce super-heated steam, Figure 1.5. Unlike PT technology, SPT solar field - receiver relative position varies

from heliostat to heliostat hindering the process of reaching a representative optical efficiency. Another difference is that SPT technologies count with a two axis tracking system.



Figure 1.4: Solar Power Tower plant [4].

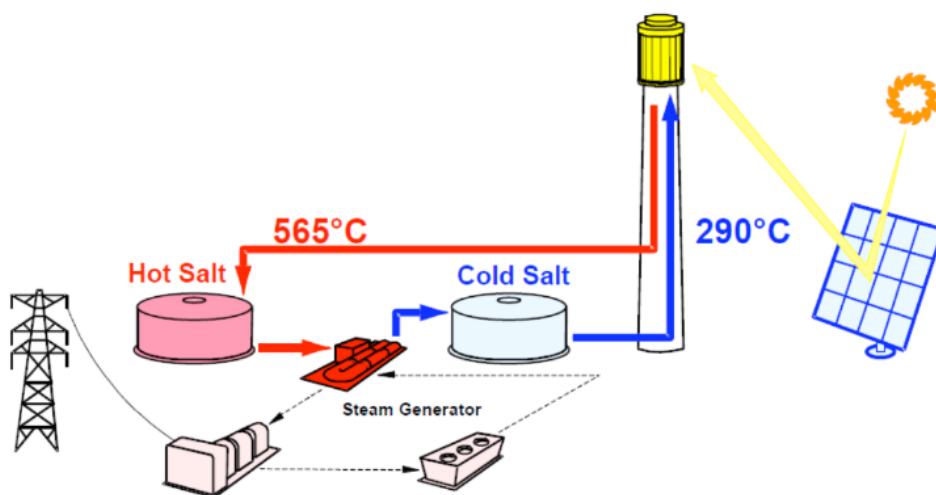


Figure 1.5: Solar Power Tower plant [5].

1.2.3 Other technologies

As stated earlier, SPT and PT are by far the concentration technologies more implemented currently and there is no reason to believe this will change, at least for the short term. However a brief description of the other existing technologies is presented.

1.2.3.1 Solar parabolic dish

According to Islam et al. [1] “In the Solar Parabolic Dish (SPD)-CSP system, a parabolic point-focus concentrator in the form of a dish is used in a system that reflects solar radiation onto a receiver at the focal point. The concentrators are placed in an assembly with a two-axis tracking system that follows the sun. At the focal point, for efficient power conversion, a Stirling/Brayton engine is placed with an electrical generator to utilize the concentrated heat on the receiver. With a concentration ratio of approximately 2000 at the focal point of the SPDes, the temperature and pressure of the working fluid generally reaches around 700–750 °C and 200 bar, respectively”. As exposed in Figure 1.10, dish is by far the less implemented technology. Figure 1.6 shows parabolic dish components and a commercial scale collector.

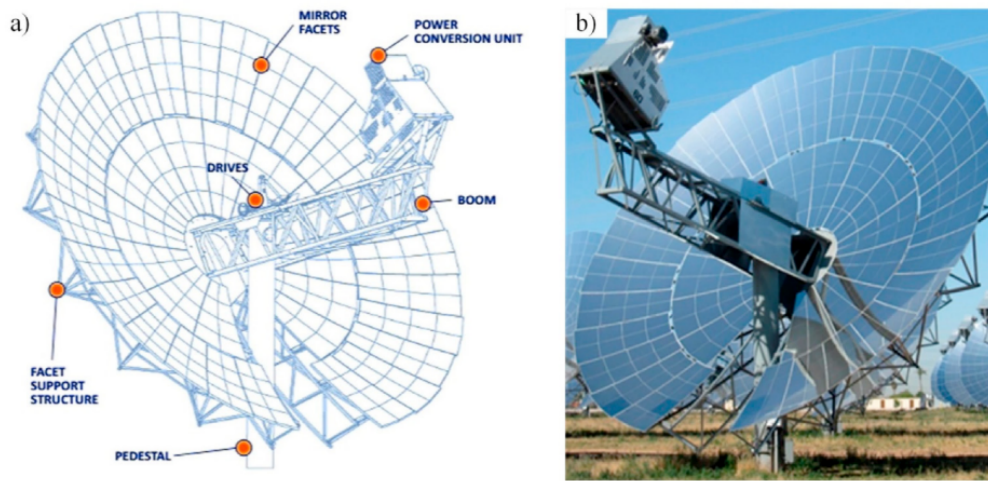


Figure 1.6: Parabolic dish technology [6].

1.2.3.2 Linear Fresnel

Linear Fresnel (LF) technologies for electricity generation consists in the arrangement of large strips of mirrors simulating a continuous concentrator. Each

1.3 Market share

CSP technologies are getting increasing attention from researchers all around the world, since they represent a renewable alternative for power or heat production that, unlike wind and photovoltaic technologies, can easily incorporate thermal storage. In their origin this power plants were implemented mainly in the United States and Spain but nowadays China and Morocco are the principal investors in this market (Fig. 1.9). It is believed that CSP plants will reach a global electricity contribution of 7% by the year 2030 and 25% by the year 2050 [1]. For these technologies to be competitive good irradiance is fundamental. Islam et al. [1] argue that viable CSP plants should operate in locations where DNI reaches values of at least $2000 \frac{kWh}{m^2 \cdot year}$. In Uruguay the available DNI in Salto reaches $1897.5 \frac{kWh}{m^2 \cdot year}$ [8]. Figures 1.9 and 1.10 show the CSP installed capacity evolution and technology distribution respectively being.

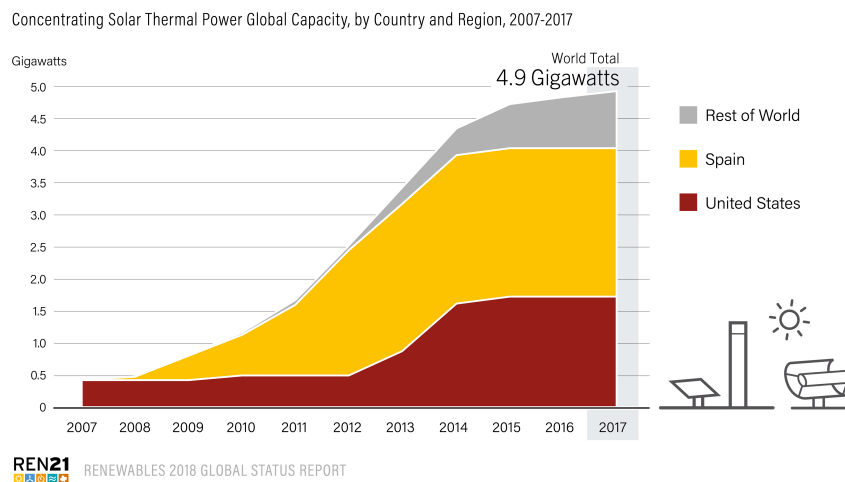


Figure 1.9: CSP Global installed capacity evolution [9].

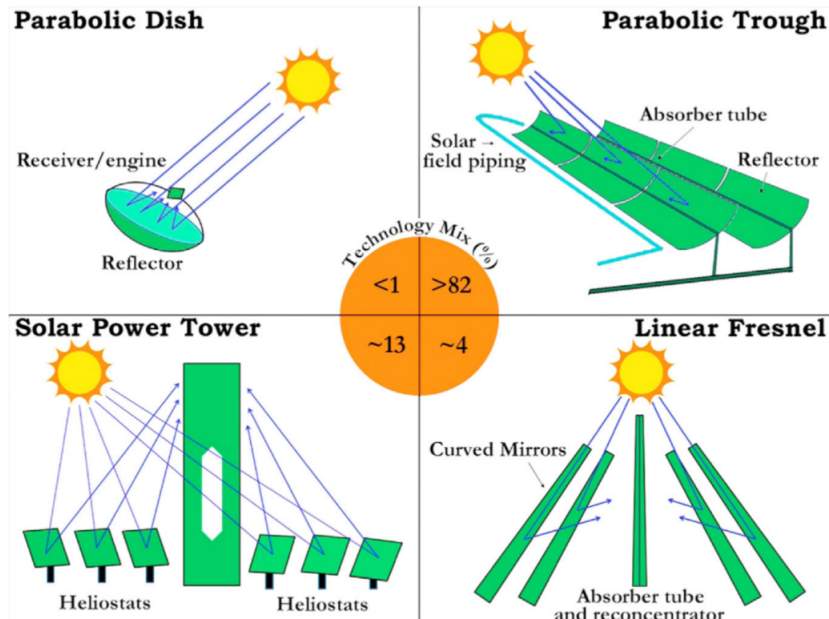


Figure 1.10: Installed CSP technologies and their market share, in 2018. [1].

In the year 2018, there were 2.2 GW under construction [1], mainly located in China due to lower investment costs and higher capacity factors making China's projects more attractive, what can be also observed by the decrease in LCOE for this region (Table 1.1 and Figure 1.11). In Figure 1.11 the yellow bars represent the range of LCOE variation for each location and the black dot the weighted average value.

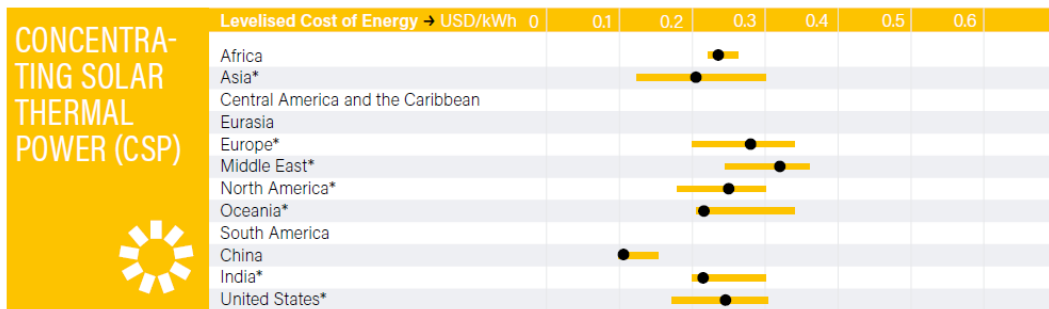


Figure 1.11: Levelized cost of energy in different locations [9].

Table 1.1: Investment cost and capacity factor of CSP technology in different locations [9].

Location	Total Investment Cost (USD/kW) 110 MW SPT		Capacity Factor	
	Min	Max	Min	Max
Africa	5.711	7.204	0.34	0.36
Asia	3.183	7.794	0.21	0.54
Europe	6.237	9.353	0.23	0.41
Middle East	6.485	6.965	0.24	0.39
North America	6.645	8.084	0.27	0.52
Oceania	6.957	6.958	0.11	0.23
China	3.272	5.695	0.32	0.62
India	3.183	7.794	0.21	0.54
United States	6.645	8.084	0.27	0.52

Moreover, due to China insertion in the market, these costs have dropped significantly during the last years, as shown in Figure 1.12. Another key aspect in the technology evolution during the last ten years is the decrease in storage costs, making large size storage capacities viable and thus, increasing the capacity factor of the plants (Figure 1.12).

Although energy prices presented are far from being competitive to other renewable technologies (Figure 1.13), when compared to fossil fuels power plants, the scenario is quite optimistic. The decision to incorporate new technologies into a certain scenario must contemplate several factors (costs, reliability, geographical distribution, among others). When considering all factors together in order to optimize the coupled system operation, the consideration of new alternatives is always beneficial, thus having available information is essential.

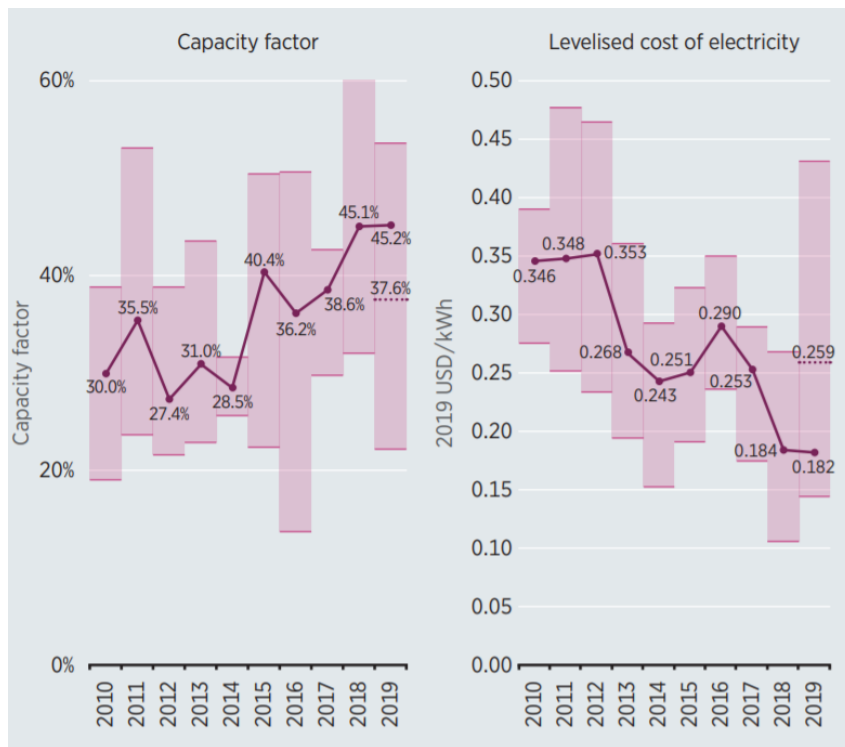


Figure 1.12: CSP capacity factor and electricity cost [10]

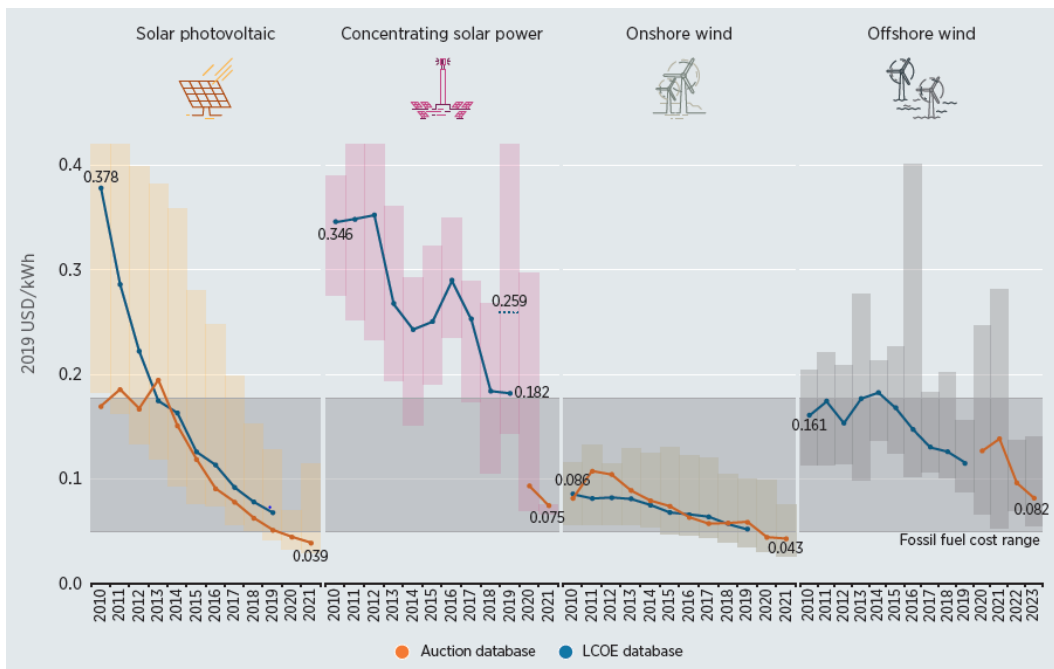


Figure 1.13: Renewable electricity price comparison [10]

1.4 Electric sector in Uruguay

According to the Dirección Nacional de Energía [11], in 2019 62% of the Uruguayan primary energy consumption was renewable, see Figure 1.14. This can be explained by the 1600 MW hydro-power installed capacity combined with a strong addition of biomass due to pulp mills projects, wind and (in lower-grade) solar technologies in the last decade. As presented in Table 1.2 hydro-power was, by far, the more significant electricity source. Particularly, 2019 was a good hydraulic year but the strong dependence on this resource can be unfavorable in dry years. Figure 1.15 shows the variation in the hydraulic energy produced considering different scenarios that vary from extra-dry (orange zone) to humid (blue zone) years. It can be seen that 2015, 2016 and 2017 have been years with good hydraulicity, favoring a more renewable energy matrix. However 2006 was a rather dry year, leading to an hydro-power generation of around 4000 GWh (around 35% of 2017). In addition, a 540MW combined cycle power plant has been recently inaugurated. In this scenario CSP technologies offer the possibility to increase the renewable share incorporating storage, a key aspect to improving the energy dispatch.

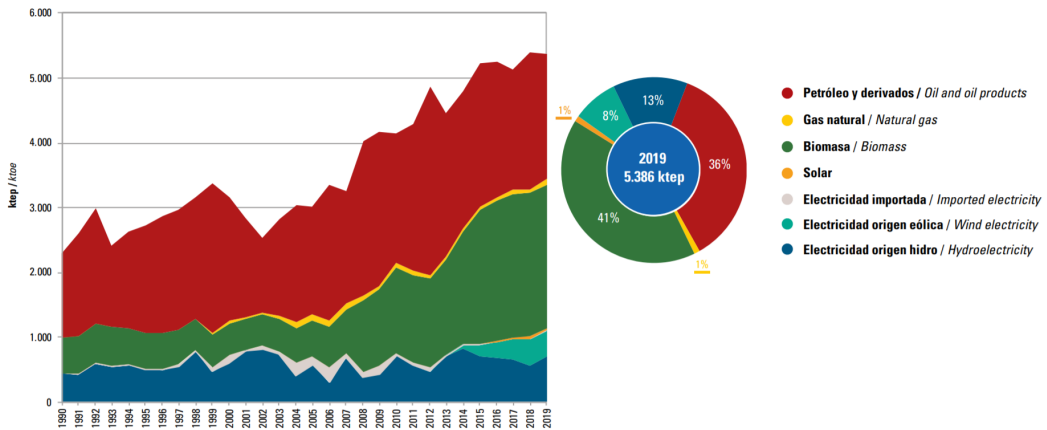


Figure 1.14: Uruguayan primary energy consumption [11].

Table 1.2: Electricity source, [11].

Source	Hydropower	Wind	Solar	Other
%	49	26	2	23

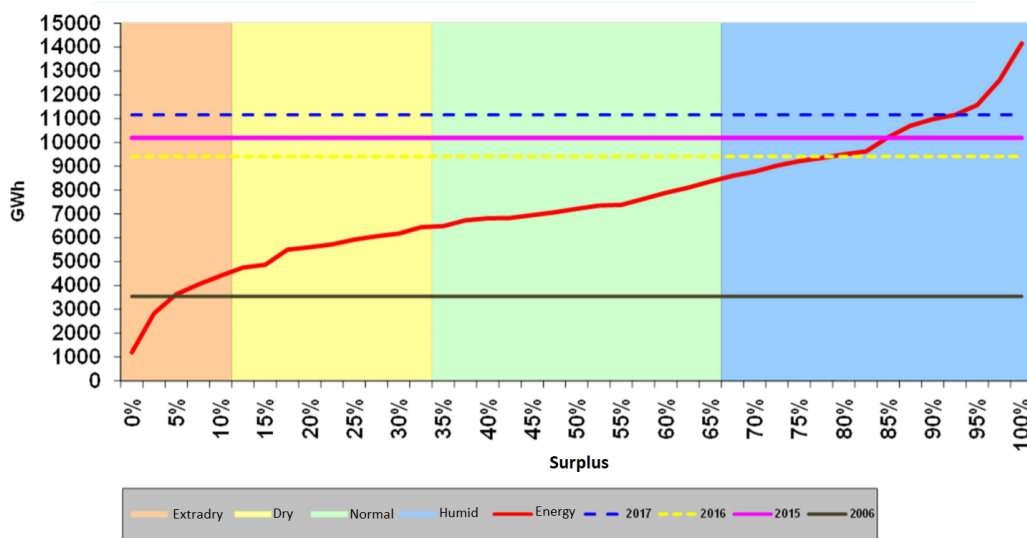


Figure 1.15: Hydropower generation different years [12].

Another key aspect to understand the future evolution of the sector is to characterize the electricity demand. The world is experiencing a great electricity consumption increase. This, combined with an increasing concern for climate change and a strong decrease in renewable technologies costs, is favoring the installation of renewable electricity sources. [9] shows that the global renewable share of electricity generation by the end of 2018 ascended to 26%.

As in the rest of the world, electricity consumption in Uruguay is increasing rapidly (see Figure 1.16) but the renewable share is considerably higher. However this increase in the demand will lead eventually to the installation of new power plants where, considering there are no more suitable locations for hydro-power plants, new technologies should be considered.

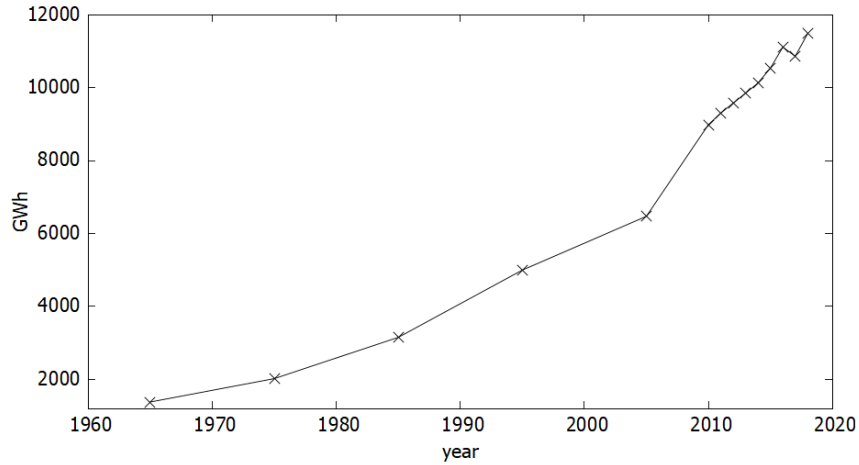


Figure 1.16: Electricity demand evolution in Uruguay, own elaboration from data obtained in [11].

1.5 Solar Resource

Regarding the irradiance available information, Uruguay has been working in the last years in creating a reliable database, this effort led to the elaboration of typical meteorological years for solar applications, considering five different locations, developed by “Laboratorio Energía Solar (LES) [13] including hourly Direct Normal Irradiance (DNI), ambient temperature and wind velocity data [13]. A brief summary of these parameters is exposed in Table 1.3 and Figure 1.17. The most suitable location for a solar project seems to be Salto (north of the country), with a relatively high solar resource, comparable to Spain irradiation where CSP plants already have been implemented. Figure 1.17 present the annual mean DNI calculated in an daily basis.

Table 1.3: Annual irradiation, mean temperature and wind speed for different locations. Data obtained from [13]

	Latitude (°)	Longitude (°)	DNI (kWh/year)	Mean ambient temperature (°C)	Mean wind Speed (m/s)
Salto	-31.27	-57.88	1897.5	19.3	4.0
Rivera	-30.90	-55.54	1779.7	18.4	3.0
Montevideo	-34.83	-56.01	1862.5	16.5	4.8
Colonia	-34.45	-57.77	1890.3	16.6	6.3
Rocha	-34.49	-54.31	1740.6	16.2	2.4

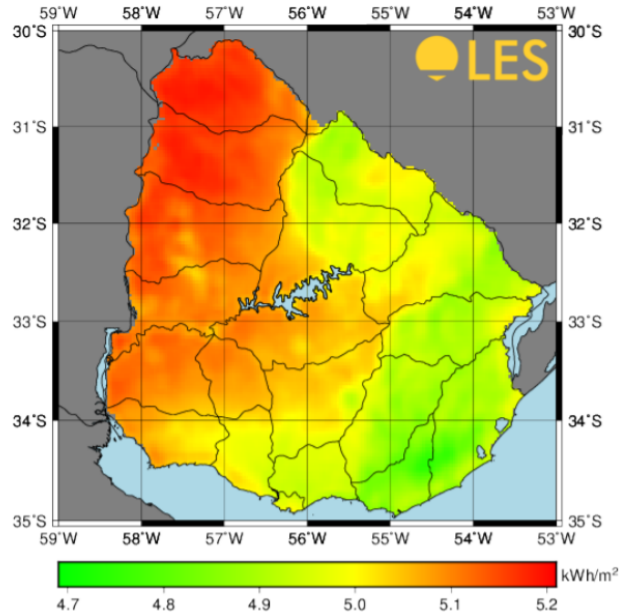


Figure 1.17: Annual average daily horizontal irradiation map [8].

1.6 Previous works and software for CSP simulation

CSP technologies are gaining attention from researchers all around the world, mainly due to their thermal storage capacity and decrease in initial investment costs. [14], [15], [16] and [17] are some examples of CSP plants feasibility studies for different countries. In the mentioned works, System Advisor Model is employed for simulations. In [14] a optimization for SPT and PT power plants is presented. Praveen et al. [15] and Tahir et al. [16] discuss the viability of PT technologies while in [17] few scenarios placed in Brazil are studied.

CSP technology potential in Uruguay has only been studied in a previous work [18] developed by SOLIDA- Energías Renovables. A non-free physic based software elaborated by SOLIDA was employed as the simulation tool. Detailed Piping and Instrumentation Diagram (*P&ID*) are available in [18]. Different configurations for both, power tower and parabolic trough technologies were studied, leading to levelized cost of energy of 142 (€/MWh) and 181.7 (€/MWh) respectively considering the most favorable scenario. Since this work was developed in 2014, a previous version of the solar data (typical meteorological year) was employed. In SOLIDA [18] a maximum storage capacity of 10 and 7.5 hours were considered for SPT and PT respectively.

In [19] several models and softwares are presented, along with each code application, strengths and weaknesses. Of the many codes presented, only four are considered total system models, this means overall performance metrics are obtained from input data (geometry, solar radiation, temperature, etc.). The total system performance softwares presented are DELSOL, SAM, SOLERGY and TRNSYS, being the most commonly employed SAM and TRNSYS.

According to Clifford K. [19]

“SAM is a free techno economic software developed by NREL that can simulate diverse scenarios including not only CSP technologies but photovoltaics systems , solar water heating, wind power plants and several other options. On the other hand, TRYNSYS is a software platform that enables the user to model different transient systems using modular components. Each component represents a physical process or feature in the system, and components can be developed and added, as needed, to a system model. A component reads in a text-based input file and provides output through the solution of algebraic or differential equations. Components include solar thermal collectors (parabolic concentrating solar collector, flat plate solar collector), heat exchangers (counter-flow, cross-flow, parallel flow, shell-and-tube, waste heat recover, etc.), thermal storage tanks (stratified, variable volume, etc.), hydraulics (pumps, pipes, valves, etc.), controllers, and more. Specific processes can be modeled for subcomponents of the total system, and total-system performance analyses can also be performed. The software contains a GUI that allows drag-and-drop arrangement and editing of component icons. Post-processing via graphing and reporting are also included in the software”.

In the current work, SAM is employed for obtaining generated energy estimations along with others results of interest presented. This selection is based in SAM reliability, user-friendly interface, available documentation, capability of modelling both SPT and PT technologies, capability of running economic analysis, software free access and short simulation duration. Furthermore, a own code for simulating PT technologies is developed and validated.

Chapter 2

Methodology

In this section a parabolic trough model developed in OCTAVE [20] is introduced. The implementation of an own code allows not only a better understanding of the process but a complete control of the processes taken into account. In addition, SAM software is introduced and the economic analysis procedure is discussed.

2.1 Parabolic trough physical modeling

Modeling of PT technologies involve various steps which are discussed below. Firstly the incident radiation over the absorber tube is estimated considering the solar relative motion to the collector. Once the incident energy is obtained the absorber tube is modeled, reaching an expression for the useful heat transferred to the HTF. At this point solving the complete HTF loop is necessary. To this end, the different components (power cycle, heat exchangers and storage tanks) are discussed. In addition, algorithms employed in the implementation of the code are presented, along with the system operation considered.

2.1.1 Solar processor

This analysis is performed considering [21] and [3]. It is essential to estimate the incident irradiation, to this end the following angles are defined (see [21]):

- Latitude (ϕ), the angular location north or south of the equator, north positive; $-90 \leq \phi \leq 90$.
- Declination (δ), the angular position of the sun at solar noon (i.e., when the sun is on the local meridian) with respect to the plane of the equator,

north positive; $-23.45 \leq \delta \leq 23.45$. This angle can be found from Equation 2.4, where n is the day of the year in question.

- Slope (β), the angle between the plane of the surface in question and the horizontal; $0 \leq \beta \leq 180$.
- Surface azimuth angle (γ), the deviation of the projection on a horizontal plane of the normal to the surface from the local meridian, with zero due south, east negative and west positive; $-180 \leq \phi \leq 180$.
- Hour angle (ω), the angular displacement of the sun east or west of the local meridian due to rotation of the earth on its axis at 15 per hour; morning negative, afternoon positive.
- Angle of incidence (θ), the angle between beam radiation on a surface and the normal to that surface.
- Zenith angle (θ_z), the angle between the vertical and the line to the sun, that is, the angle of incidence of beam radiation on a horizontal surface.
- Solar altitud angle (α_s), the angle between the horizontal and the line to the sun, that is, the complement of the zenith angle.
- Solar azimuth angle (γ_s), the angular displacement from south of the projection of beam radiation on the horizontal plane. Displacements east of south are negative and west of south are positive.

It is also crucial to define the solar time which is defined as the time based on the apparent angular motion of the sun across the sky, with solar noon the time the sun crosses the meridian of the observer [21]. This parameter can be expressed as follows (Equation 2.1) where t_s is the solar time, t_{std} the standard time in the zone consider, L_{std} the standard meridian for the local time zone, L_{loc} the longitude of the location in question and E a correction factor that depends on the day of the year n (see Equation 2.2).

$$t_s - t_{std} = 4(L_{std} - L_{loc}) + E \quad (2.1)$$

$$E = 229.2(0.000075 + 0.001868 \cos\left((n-1)\frac{360}{365}\right) - 0.032077 \sin\left((n-1)\frac{360}{365}\right) - 0.014615 \cos\left(2(n-1)\frac{360}{365}\right) - 0.04089 \sin\left(2(n-1)\frac{360}{365}\right)) \quad (2.2)$$

To be able to calculate the incidence angle θ the auxiliary hour, declination, zenith and solar azimuth angles as defined in the beginning of this section must be determined. To this end the following Equations are employed (2.3, 2.4, 2.5, 2.6)

$$\omega = (t_s - 12)15 \quad (2.3)$$

$$\delta = 23.45 \sin \left(360 \frac{284 + n}{365} \right) \quad (2.4)$$

$$\cos(\theta_z) = \cos(\phi) \cos(\delta) \cos(\omega) + \sin(\phi) \sin(\delta) \quad (2.5)$$

$$\gamma_s = \text{sign}(\omega) \left| \arccos \left(\frac{\cos(\theta_z) \sin(\phi) - \sin(\delta)}{\sin(\theta_z) \cos(\phi)} \right) \right| \quad (2.6)$$

In addition, parabolic trough technology allows a one axis tracking that can be oriented in any direction, being the most commonly used the east-west tracking (north-south axis orientation). To consider the orientation a new parameter (γ_{col}) is defined. This angle can be either 90 when $\gamma_s > 0$ or -90 if $\gamma_s \leq 0$. Finally the incidence angle is presented.

$$\theta = \arccos(\sqrt{1 - (\cos(\theta_e) - \cos(\theta_e)(1 - \cos(\gamma_s - \gamma_{col})))^2}) \quad (2.7)$$

When considering a entire solar field, shadowing between structures must also be considered for every time step. ω_{col} and $\eta_{shadior}$ are defined as follows (see Figure 2.1 and Equations 2.8 - 2.9). $\eta_{shadior}$ represents the fraction of the collector that is not receiving solar irradiation due to the shadow of the contiguous collector.

$$\omega_{col} = \arctan \left(\frac{\cos(\theta_e) \sin(\gamma_s - \gamma_{col})}{\sin(\theta_e)} \right) \quad (2.8)$$

$$\eta_{shadow} = |\cos(\omega_{col})| \frac{d}{w} \quad (2.9)$$

where d is the distance between collectors and w their width. At this point the irradiation over the collector is estimated, however to calculate the absorbed energy optical properties of collectors and receivers must be taken into account. These properties vary with the direction of irradiation, making the calculation process more difficult. For taking into account this phenomena the incident angle modifier (IAM) is defined as the ratio of the properties in any given direction and the properties normal to the surface (Equation 2.10).

$$IAM = a_0 + a_1 \frac{\theta}{\cos(\theta)} + a_2 \frac{\theta^2}{\cos(\theta)} \quad (2.10)$$

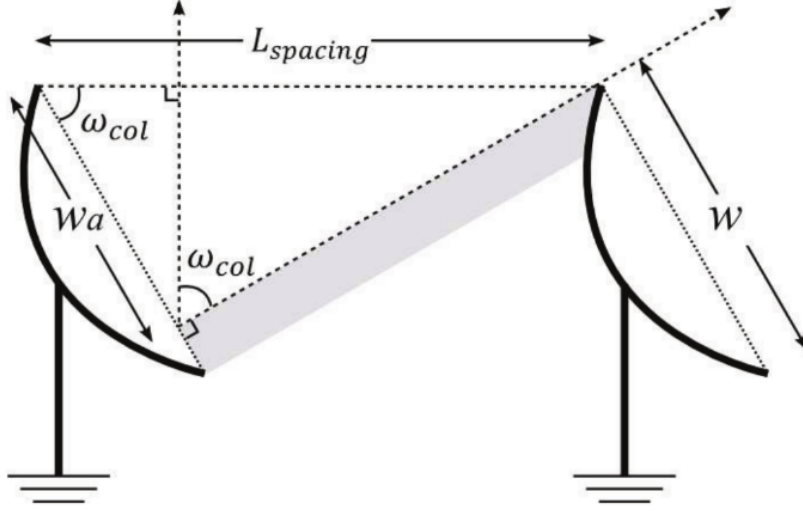


Figure 2.1: Shadowing between structures [3].

where a_0 , a_1 and a_2 are constants associated with the considered collector and θ is in radians. Finally, the absorbed radiation per unit surface area can be expressed as follows (Equation 2.11)

$$S'' = G \cos(\theta) I A M \rho_{mirror} \gamma_{int} \tau_{glass} \alpha_{tube} c f \eta_{shadow} \quad (2.11)$$

In Equation 2.11 G is the incident radiation ($\frac{W}{m^2}$), ρ_{mirror} , γ_{int} , τ_{glass} , α_{tube} and $c f$, represent the mirror reflectivity, deviation in the position of the receiver tube from the optical focus, glass transmissivity, tube absorptivity and cleanness factor respectively.

2.1.2 Absorber tube modeling

In this section, a physical approach to solving the absorber is described. Figure 2.2 presents a qualitative scheme of this problem. The main energy input is situated in the absorber where part of the incident radiation is absorbed, however the glass is not completely transparent leading to a smaller energy input in that surface. A fraction of the absorbed energy is transferred to the fluid while the rest is lost to the environment. In this work heat refers to thermal power (\dot{Q} or S [W]). In addition, the notation \dot{Q}' and \dot{Q}'' allude to the magnitude \dot{Q} per unit of length or area, respectively. For thermal resistances, the notation R' refer to $[\frac{mK}{W}]$.

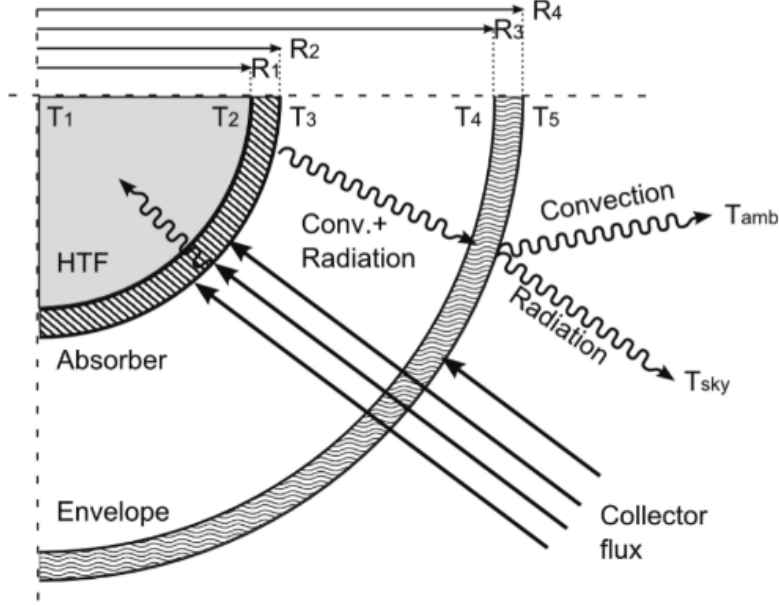


Figure 2.2: Heat flows in Parabolic Trough collectors [3].

A useful tool for a better understanding of the problem is to build an electric equivalent diagram to schematize the different heat transfer phenomena taken into account. The scheme is presented below (Figure 2.3) where T_1 represents the fluid temperature, T_2 the interior absorber temperature, T_3 the exterior absorber temperature, T_4 the interior glass temperature, T_5 the exterior glass temperature, T_6 the ambient temperature and T_7 the sky temperature used for radiation exchange. \dot{Q}'_u is the heat transferred to the HTF, \dot{Q}'_{rc} and R'_{rc} the heat transferred from the outer receptor surface to the collector envelope and R'_{rc} the equivalent resistance associated (see Equation 2.12). Finally, \dot{Q}'_{loss} is the power lost to the ambient.

$$\dot{Q}'_{rc} = \frac{T_3 - T_5}{R'_{rc}} \quad (2.12)$$

For calculating each resistance the associated transfer coefficients must be known, to this end the following correlations are presented [22]. The fluid gains heat due to its convection exchange with the hot tube (\dot{Q}'_u). This useful heat can be calculated employing Newton's law of cooling (Equation 2.13) where D_2 is the absorber diameter. The heat transfer coefficient h_1 can be expressed

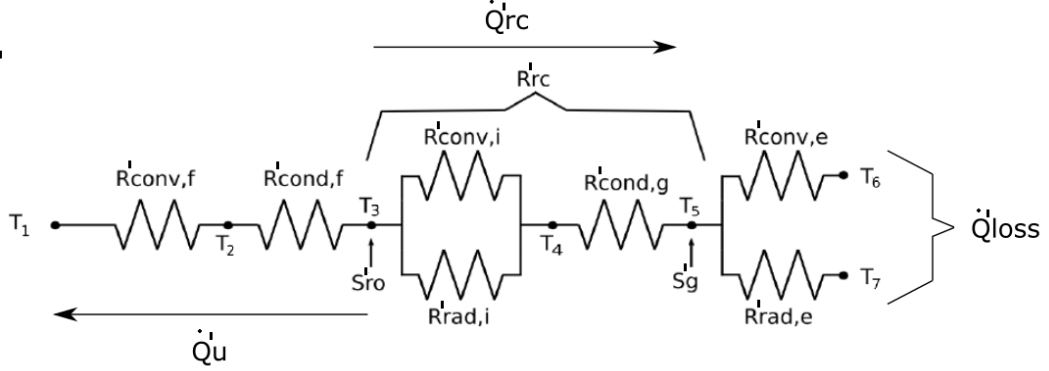


Figure 2.3: Resistance diagram, own elaboration.

as function of the Nusselt number (Equation 2.14).

$$\dot{Q}'_u = \pi D_2 h_1 (T_2 - T_1) \quad (2.13)$$

$$h_1 = Nu_{D2} \frac{k_1}{D_2} \quad (2.14)$$

Using this correlation for Nusselt number.

$$Nu_{D2} = \frac{f_2 (Re_{D2} - 1000) Pr_1}{1 + 12.7 \sqrt{f_2} (Pr_1^{\frac{2}{3}} - 1)} \left(\frac{Pr_1}{Pr_2} \right)^{0.11} \quad (2.15)$$

where Pr_1 and Pr_2 are the Prandlt number at T_1 and T_2 respectively, and f_2 is calculated by

$$f_2 = (0.79 \ln(Re_{D2}) - 1.64)^{-2} \quad (2.16)$$

Equation 2.13 presents the heat gained by the thermal fluid (\dot{Q}'_u), however to determine this value T_2 must be known what means that every resistance must be calculated. The following Equations provide expressions for the different heat rates being \dot{Q}'_{23} the conduction transfer in the tube, $\dot{Q}'_{34,rad}$ and $\dot{Q}'_{34,conv}$ the radiation and convection heat exchange between the tube and the glass respectively.

$$\dot{Q}'_{23} = 2\pi k_{23} \left(\frac{T_2 - T_3}{\ln\left(\frac{D_3}{D_2}\right)} \right)$$

$$\dot{Q}'_{34,rad} = \frac{\pi D_3 \sigma (T_3^4 - T_4^4)}{\frac{1}{\varepsilon_3} + \frac{(1-\varepsilon_4)D_3}{\varepsilon_4 D_4}}$$

$$\dot{Q}'_{34,conv} = \pi D_3 h_{34} (T_3 - T_4)$$

As the tube-glass convection is under vacuum conditions, the convection heat transfer between the absorber and glass envelope is associated with the free-molecular convection (see Equation 2.17 and 2.18 for determining the h_{34} heat transfer coefficient) ([22]).

$$h_{34} = \frac{k_{std}}{\frac{D_3}{2 \ln(\frac{D_4}{D_3})} + b \lambda (\frac{D_3}{D_4} + 1)} \quad (2.17)$$

$$\lambda = \frac{2.33 \times 10^{-20} (T_{34} + 273.15)}{P_a \delta^2} \quad (2.18)$$

Where k_{std} , b , λ and δ for air are presented in table 2.1. On the other hand P_a is the annulus gas pressure (*mmHg*).

Table 2.1: Air properties [22]

Gas	k_{std}	b	λ (cm)	γ	δ (cm)
Air	0.02551	1.571	88.67	1.39	3.53e-8

Finally the conduction through the glass, its convection and radiation exchange can be expressed as follows by the Equations 2.19, 2.21 and 2.20.

$$\dot{Q}'_{45,cond} = 2\pi k_{45} \frac{(T_4 - T_5)}{\ln \frac{D_5}{D_4}} \quad (2.19)$$

$$\dot{Q}'_{57,rad} = \pi D_5 \varepsilon_5 \sigma (T_5^4 - T_7^4) \quad (2.20)$$

$$\dot{Q}'_{56,conv} = \pi D_5 h_{56} (T_5 - T_6) \quad (2.21)$$

$$h_{56} = Nu_{D_5} \frac{k_{56}}{D_5}$$

$$Nu_{D_5} = C Re_{D_5}^m Pr_6^n \left(\frac{Pr_6}{Pr_5} \right)^{0.25}$$

Where C , m and n are constant that depend on the Reynolds (C and m) or Prandtl number (n) as presented in Tables 2.2 and 2.3.

Figure 2.2 scheme can be used in any cross section of the absorber tube, however different axial positions lead to different temperatures varying the convective coefficients, the resistance involved in the heat calculation and consequently the local heat transfer to the fluid. For solving the problem it is necessary to incorporate the following balance equation for the fluid where \dot{m}

Table 2.2: C and m constants for determining Nusselt coefficient as function of Reynolds number [22].

Re_D	C	m
1-40	0.75	0.4
40-1000	0.51	0.5
1000-200000	0.26	0.6
200000-1000000	0.076	0.7

Table 2.3: n constant for determining Nusselt coefficient as function of Prandtl number [22].

	$Pr \leq 10$	$Pr > 10$
n	0.37	0.36

is the mass flow rate and Cp the specific heat. Assuming steady state conditions, Equation 2.22 is reached.

$$\dot{m}Cp\frac{\partial T_f}{\partial x} = \dot{Q}'_u \quad (2.22)$$

Considering the circuit (Figure 2.3) the heat transferred between the absorber outlet temperature (T_3) and the external glass surface (T_5) can be expressed as presented in Equation 2.12.

In a steady-state condition, an energy balance to the receptor and its cover can be expressed as shown in Equations 2.23 and 2.24 respectively where S'_g and S'_{ro} are the solar energy absorbed terms for the glass and receiver respectively.

$$S'_g + \dot{Q}'_{rc} = \frac{T_5 - T_6}{R'_{conv,e}} + \frac{T_5 - T_7}{R'_{rad,e}} \quad (2.23)$$

$$\frac{T_3 - T_1}{R'_{conv,f} + R'_{cond,f}} + \dot{Q}'_{rc} = S'_{ro} \quad (2.24)$$

where $R'^*_{rad,e}$ can be expressed as follows (Eq.2.25)

$$R'^*_{rad,e} = \frac{1}{\sigma \varepsilon_5 \pi D_5 (T_5^2 + T_7^2)(T_5 + T_7)} \quad (2.25)$$

It is useful to define a new radiative resistance from the glass to the ambient as follows in Equation 2.26

$$R'^*_{rad,e} = R'_{rad,e} \frac{T_5 - T_6}{T_5 - T_7} \quad (2.26)$$

Rearranging Equation 2.23, Equation 2.27 can be reached. Considering the new radiative resistance 2.26 and Equation 2.27, 2.28 is obtained. In order to simplify the notation, R'_{ext} is defined as the equivalent resistance correspondent to the external glass to ambient heat exchange 2.29.

$$S'_g R'_{conv,e} + \dot{Q}'_{rc} R'_{conv,e} = T_5 - T_6 + \frac{R'_{conv,e}}{R'_{rad,e}} (T_5 - T_7) \quad (2.27)$$

$$S'_g + \dot{Q}'_{RC} = \frac{T_5 - T_6}{R'_{ext}} \quad (2.28)$$

$$R'_{ext} = R'_{conv,e} || R'^*_{rad,e} \quad (2.29)$$

where

$$R'_{conv,e} || R'^*_{rad,e} = \frac{1}{\frac{1}{R'_{conv,e}} + \frac{1}{R'^*_{rad,e}}}$$

On the other hand, from Equation 2.12, an expression for T5 can be obtained

$$T_5 = -\dot{Q}'_{rc} R'_{rc} + T_3 \quad (2.30)$$

Combining 2.30, 2.28 and 2.29 Equation 2.31 can be found.

$$S'_g R'_{ext} + \dot{Q}'_{rc} R'_{ext} = T_3 - \dot{Q}'_{rc} R'_{rc} - T_6 \quad (2.31)$$

The final step is to eliminate the T_3 dependence, with the objective of reaching an expression that only involves fluid and ambient temperatures¹. To this end, Equation 2.24 and 2.31 are employed leading to Equation 2.32.

$$\dot{Q}'_{rc} (R'_{ext} + R'_{rc}) = T_1 - T_6 + (S'_{ro} - \dot{Q}'_{rc}) (R'_{conv,f} + R'_{cond,f}) - S'_g R'_{ext} \quad (2.32)$$

Defining $\sum R'$ as follows and rearranging, Equation 2.32 can be re-written 2.34

$$\sum R' = R'_{ext} + R'_{rc} + R'_{conv,f} + R'_{cond,f} \quad (2.33)$$

$$\dot{Q}'_{rc} \sum R' = T_1 - T_6 + S'_{ro} (R'_{conv,f} + R'_{cond,f}) - S'_g R'_{ext} \quad (2.34)$$

¹Sky temperature is considered in $\sum R'$ by R'_{ext} (see Equations 2.26, 2.29 and 2.33)

Equations 2.35 and 2.36 present the energy balance for the collector and glass cover respectively

$$S'_{ro} + S'_g - \dot{Q}'_{loss} = \dot{Q}'_u \quad (2.35)$$

$$\dot{Q}'_{loss} = S'_g + \dot{Q}'_{rc} \quad (2.36)$$

leading to Equation 2.37

$$\dot{Q}'_{rc} = S'_{ro} - \dot{Q}'_u \quad (2.37)$$

Finally combining 2.34 and 2.37, the useful heat power \dot{Q}'_u Equation 2.38 is reached.

$$\dot{Q}'_u = S'_{ro} \left[1 - \frac{(R'_{conv,f} + R'_{cond,F})}{\sum R'} \right] + S'_g \frac{R'_{ext}}{\sum R'} - \frac{(T_1 - T_6)}{\sum R'} \quad (2.38)$$

For convenience, A is defined as the term independent of T_1 (constant in each time step), see Equation 2.39

$$A = S'_{ro} \left[1 - \frac{(R'_{conv,f} + R'_{cond,F})}{\sum R'} \right] + S'_g \frac{R'_{ext}}{\sum R'} \quad (2.39)$$

At this point, using the expression 2.38 for the useful heat transferred to the fluid (\dot{Q}'_u), the differential Equation 2.22 can be solved leading to an expression of the outlet temperature as function of the distance traveled by the fluid Equation 2.42. The step by step procedure is presented below.

$$\frac{\partial T_1}{\partial x} = \frac{\dot{Q}'_u}{\dot{m}C_p}$$

$$\dot{Q}'_u = A - \frac{(T_1 - T_6)}{\sum R'}$$

$$\frac{\partial T_1}{\partial x} = \frac{1}{\dot{m}C_p} \left(A - \frac{T_1 - T_6}{\sum R'} \right)$$

An auxiliary variable θ is defined by Equation 2.40

$$\theta = \frac{(T_1 - T_{inf})}{\sum R'} - A \quad (2.40)$$

$$\frac{\partial \theta}{\partial x} = \frac{\partial T_1}{\partial x} \frac{1}{\sum R'}$$

Incorporating this variable to the differential equation and solving

$$\frac{\partial \theta}{\partial x} = -\frac{\theta}{\dot{m}C_p \sum R'}$$

$$\theta_o = \theta_i e^{-\frac{L}{\dot{m}C_p \sum R'}} \quad (2.41)$$

$$T_o = \sum R' A (1 - e^{-\frac{L}{\dot{m}C_p \sum R'}}) + (T_i - T_6) e^{-\frac{L}{\dot{m}C_p \sum R'}} + T_6 \quad (2.42)$$

Equation 2.42 is employed for calculating the outlet HTF temperature (T_o) from the inlet (T_i), ambient (T_6) and sky temperature along with irradiation data.

2.1.3 Solar field solver algorithm

The approach considered to solve the problem presented in section 2.1.2 is now discussed. The first step consists in adding hourly information of meteorological data (such as DNI, ambient temperature, wind velocity) and nominal parameters of the problem (solar field HTF inlet and outlet temperature, storage capacity, optical factors and typical values of heat transfer coefficients).

Once this information is loaded the heat hourly gained by the absorber tube is calculated. At this point an iterative procedure is started in order to obtain the HTF fluid mass flow that can be heated up to the desired outlet temperature under these conditions. Typically the previous step mass flow is employed to calculate a first approximation of the heat transfer coefficients. Once these coefficients are obtained Equation 2.43 (derived from Equation 2.41) is employed to re-calculate the circulating mass flow considering the new ambient conditions, this process is repeated until the mass flow calculated in two consecutive iterations are sufficiently close.

$$\dot{m} = \frac{-L}{\ln\left(\frac{T_o - T_6 - \sum RA}{T_i - T_6 - \sum RA}\right) C_p \sum R} \quad (2.43)$$

To this point, no discretization was employed leading to unique absorber resistances, $\sum R'$ and $\sum R' A$ values for each time step. Since the HTF temperature increase around $100^\circ C$ inside the collector, convective coefficients and absorber temperature vary in the axial direction. As an improvement the absorber tube is discretized leading to a better representation of the real phenomenon, considering N tube partitions and solving Equation 2.42 for each

partition in order to obtain the following section inlet temperature. This approach leads to different absorber resistances in each partition improving the thermal losses calculation. Starting from the one node approximation calculated mass flow, the new discrete problem is solved in order to reach the desired HTF outlet temperature in the last partition. If the aimed temperature is obtained the process is finished, otherwise the mass flow rate is changed until this condition is fulfilled leading to a solution that takes into account the difference in the heat losses due to the absorber temperature distribution. Figure 2.4 shows a scheme of the solver implementation where M_{htf} is the HTF mass flow, $M_{htf,n}$ is the following iteration step HTF mass flow, $T_{out,N}$ is the temperature obtained at the outlet of the last node and T_{imp} is de setted designed solar field outlet temperature.

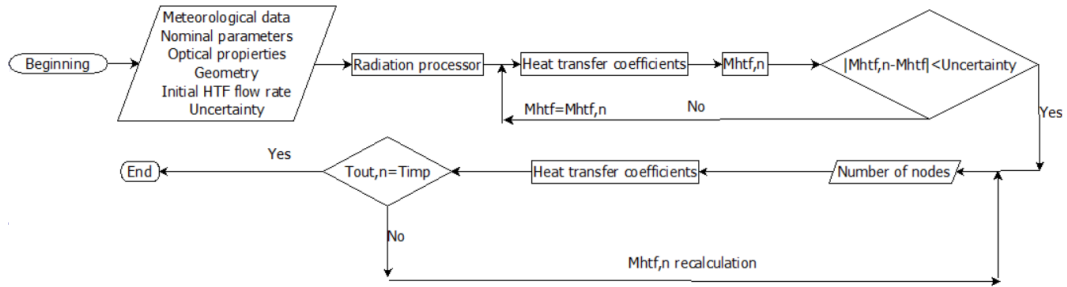


Figure 2.4: Solar field algorithm scheme, own elaboration.

2.1.4 Power cycle implementation

In CSP plants a rankine cycle is usually employed. The original cycle typically consists in a steam generator, turbine, condenser and pump. When leaving the steam generator, the steam is preferred in a super-heated condition in order to avoid erosion problems in the turbine blades and increase the cycle efficiency. Moreover, for energy applications, in order to increase the cycle efficiency the following adaptations are usually considered.

- Reheating: The steam expansion is separated in two consecutive stages. After leaving the first expansion stage, the steam is heated up to nearly the high pressure turbine inlet temperature.
- Regenerative feed water heating: After leaving the condenser the water is at low temperatures (around $30^{\circ}C$). An efficiency improvement

consists in heating up this water before it reaches the steam generator, reducing the irreversibilities. A fraction of the steam turbine is extracted and employed to heat the water in either open or closed heat exchangers. Typically more than one extraction is performed.

Figure 2.5 shows a typical Rankine cycle with the mentioned improvements being T_A and T_B the high and low pressure turbine stages respectively, C the condenser, PA the water pre-heater, Des the deaerator and GV the steam generator.

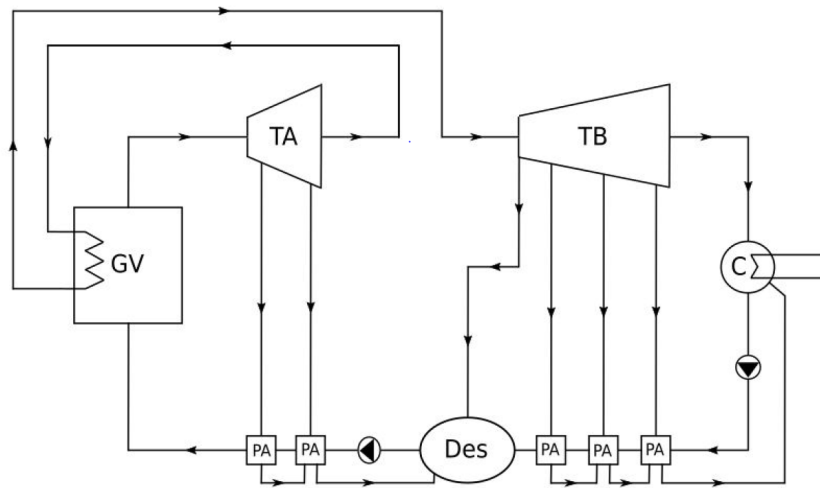


Figure 2.5: Typical generation plant power block. T_A and T_B are the high and low pressure turbine stages respectively, C the condenser, PA the water pre-heater, Des the deaerator and GV the steam generator, own elaboration.

In this work the cycle efficiency is the crucial parameter, used to obtain the electric energy produced from the total heat exchanged between the HTF and the steam. At nominal conditions the extraction pressures are determined and, knowing the steam evolution curve, the extracted steam temperature can be found. Each turbine stage working in designed conditions is characterized by an isentropic efficiency (refer to Equation 2.44).

However, when working at part-load conditions both, the extraction pressures and stage isentropic efficiency vary, causing a change in the steam inlet temperature entering the feed water pre-heaters and hindering the calculation process since the strong coupling of the entire cycle. In addition, the necessary turbine information for this process (isentropic efficiency of stages, steam evolution curve, nominal extraction pressures) is not usually accessible for researchers.

$$\eta = \frac{h_{steam,in} - h_{steam,out}}{h_{steam,in} - h_{steam,out,S}} \quad (2.44)$$

In order to solve this problem, the approach considered by Montes et al. [23] is taken into account. In the mentioned work, the turbine part load efficiency is calculated as in Equation 2.45, being *Red* a parameter that depends on the circulating mass flow (Equation 2.46). For calculating the pressure drop at part load conditions in a turbine stage, the control method must be defined. Montes et al. [23] employs the sliding pressure method which consists in fixing the inlet turbine temperature decreasing the inlet pressure. Under this consideration Equation 2.47 express the mentioned pressure drop as a function of the mass flow rate.

$$\eta_{turbine} = (1 - Red) \eta_{turbine,D} \quad (2.45)$$

$$Red = 0.191 - 0.409 \left(\frac{\dot{m}}{\dot{m}_{ref}} \right) + 0.218 \left(\frac{\dot{m}}{\dot{m}_{ref}} \right)^2 \quad (2.46)$$

$$\frac{P_1^2 - P_2^2}{P_{1,ref}^2 - P_{2,ref}^2} = \left(\frac{\dot{m}}{\dot{m}_{ref}} \right)^2 \quad (2.47)$$

where P_1 is the turbine inlet pressure and P_2 the turbine outlet pressure. The subscript *ref* refer to the nominal working conditions. For heat exchangers the following considerations are taken into account.

$$\frac{UA}{UA_{ref}} = \left(\frac{\dot{m}}{\dot{m}_{ref}} \right)^{0.8} \quad (2.48)$$

$$\Delta P = k\dot{m}^2 \quad (2.49)$$

A first approach to solve the behavior of the power cycle at part load conditions is presented. Knowing the available HTF flow rate, the generated steam is firstly estimated as in Equation 2.50.

$$\dot{m} = \dot{m}_{ref} \left(\frac{\dot{m}_{HTF}}{\dot{m}_{HTF,ref}} \right) \quad (2.50)$$

Considering T_A and T_B as a unique turbine and P_2 (TB outlet pressure) fixed by the condenser temperature, P_1 (TA inlet pressure) can be estimated by Equation 2.47. As P_1 changes, the extractions pressures (P_{ext}) (hence extractions temperatures) vary. Due to the limited information available, no data about the nominal extraction pressures could be found. In addition, no information about isentropic efficiency for each stage was founded. Considering these uncertainties it is not possible to determine the extraction state, thus the water pre-heaters could not be modeled adequately making this approach not viable.

Considering that [23] considers the same cycle configuration and capacity as in Figure 2.5 (for a 55MW PT plant), the efficiency- mass flow rate relation obtained in the mentioned work is employed (Figure 2.6).

2.1.5 Heat exchanger

This section focus on the approach that is employed for solving the HTF-steam and HTf-salts heat exchangers. In this work, the effectiveness (ε) is employed to characterize the heat exchangers [24]. This parameter represents the actual heat transfer rate between the hot (h) and cold (c) fluids over the maximum possible heat transfer rate, Equation 2.51. It is also necessary to define de heat capacitance for both the hot and cold fluid, C_h and C_c , Equation 2.52 and 2.53.

$$\varepsilon = \frac{\dot{Q}}{\dot{Q}_{max}} \quad (2.51)$$

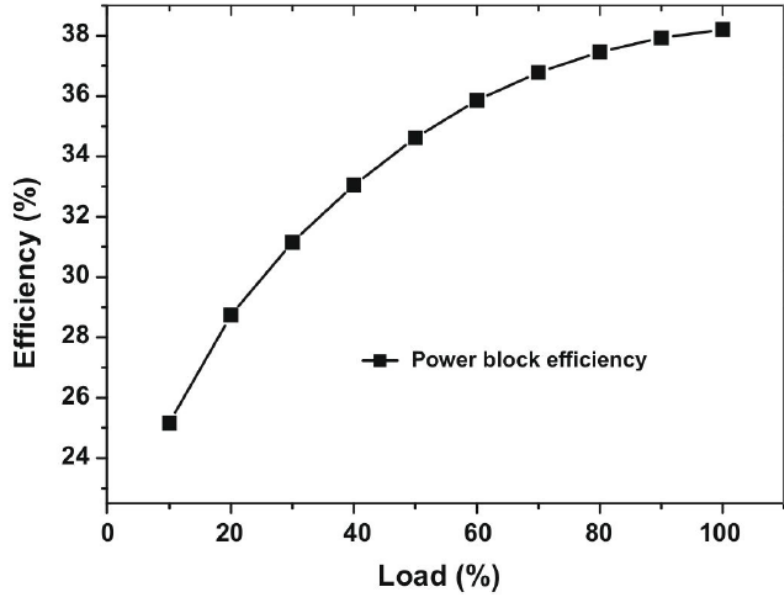


Figure 2.6: Power block efficiency [23]

$$C_h = \dot{m}_h C p_h \quad (2.52)$$

$$C_c = \dot{m}_c C p_c \quad (2.53)$$

where \dot{Q} is the heat transferred from hot fluid to cold and can be calculated from an energy balance to the hot or cold fluid (Equation 2.54) and \dot{Q}_{max} can be obtained by Equation 2.55.

$$\dot{Q} = \dot{m}_h C p_h \Delta T_h = \dot{m}_c C p_c \Delta T_c \quad (2.54)$$

$$C_{min} = \min(C_h, C_c)$$

$$C_{max} = \max(C_h, C_c)$$

$$\dot{Q}_{max} = C_{min}(T_{h,in} - T_{c,in}) \quad (2.55)$$

In addition, each heat exchanger effectiveness can be expressed as a function of two dimensionless parameter (Equation 2.56)

$$\varepsilon = f(NTU, Cr) \quad (2.56)$$

with

$$NTU = \frac{UA}{C_{min}}$$

$$UA = \frac{1}{\frac{1}{h_h A_h} + \frac{1}{h_c A_c}}$$

where C_r is obtained by Equation 2.57

$$Cr = \frac{C_{min}}{C_{max}} \quad (2.57)$$

Where h_h , A_h , h_c and A_c are the heat transfer coefficients and transfer area for the hot and cold fluid respectively. The heat transfer coefficients are assumed to be proportional to the mass flow rate circulating, raised to the power of 0.8 ($m^{0.8}$), Equation 2.58. From Equation 2.58 the following relation between UA at nominal conditions and any other condition is calculated by Equation 2.59

$$h \propto m^{0.8} \quad (2.58)$$

$$UA = \frac{1}{\frac{1}{h_h A_h} \left(\frac{\dot{m}_{h,nom}}{\dot{m}_h}\right)^{0.8} + \frac{1}{h_c A_c} \left(\frac{\dot{m}_{c,nom}}{\dot{m}_c}\right)^{0.8}} \quad (2.59)$$

HTF-steam heat exchanger

For this application the HTF-steam heat exchanger is sub-divided in 3 different sections (pre-heater, steam generator and super-heater, see Figure 2.7). The SIEMENS SST-700 nominal steam mass flow ($54.3 \frac{kg}{s}$) is considered for the analysis. Each section is modeled by its global exchange coefficient (UA) that is calculated from nominal temperatures and flows rates.

The nominal efficiency is calculated from the temperatures presented in Figure 2.7 and Equation 2.60 where ΔT_{max} and ΔT_{in} are the temperature variation for the fluid with lower heat capacitance and the difference between both fluids inlet temperature.

$$\varepsilon = \frac{\Delta T_{max}}{\Delta T_{in}} \quad (2.60)$$

Considering counterflow heat exchangers [24], NTU can be obtained from expressions 2.61 and 2.62 for $Cr < 1$ and $Cr = 0$.

$$NTU = \frac{1}{Cr - 1} \ln \left(\frac{\varepsilon - 1}{\varepsilon Cr - 1} \right) \quad (2.61)$$

$$NTU = -\ln(1 - \varepsilon) \quad (2.62)$$

When the cycle is operating in any other condition UA , NTU , C_{min} and Cr are adjusted leading to a new efficiency (Equation 2.56), heat exchanged and HTF outlet temperature. To correct UA the approximation presented in 2.63 is employed.

$$\frac{\dot{m}_{HTF}}{\dot{m}_{HTF,nom}} = \frac{\dot{m}_{steam}}{\dot{m}_{steam,nom}} \quad (2.63)$$

Incorporating this consideration to Equation 2.59, Equation 2.64 is reached. The importance of modeling this component lies in a correct calculation of the HTF cold temperature (heat exchanger outlet and solar field inlet) at not nominal conditions.

$$UA = UA_{nom} \left(\frac{\dot{m}_{HTF}}{\dot{m}_{HTF,nom}} \right)^{0.8} \quad (2.64)$$

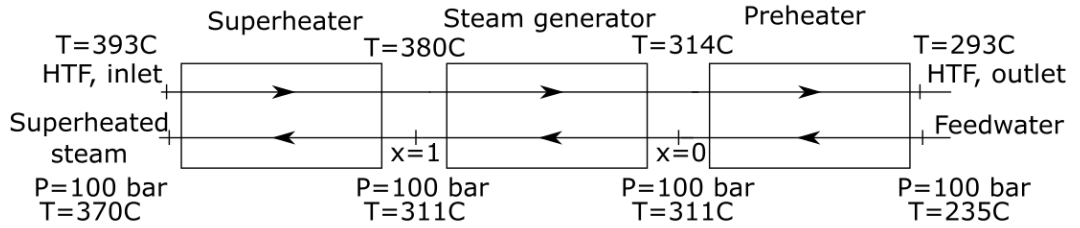


Figure 2.7: HTF-steam heat exchanger, own elaboration

2.1.6 Storage

A two tank salt storage system is implemented. The hot and cold tank temperatures are 386°C and 290°C respectively. The solar field is over-sized in order to allow that at good irradiance conditions the HTF heated exceed the

necessary mass flow to generate the steam. This excess circulates through a HTF-salt heat exchanger heating the salts up to the desire temperature. The salts are stored in the tank to be used in least favorable solar conditions afterwards, when the flows through the heat exchanger is inverted and the HTF is heated by the salts.

Once again the HTF-salt heat exchanger is represented by a typical (UA) , value that is corrected when not operating at nominal flow rates. Regarding the thermal losses, the tanks are considered to be adiabatic.

This heat exchanger is solved in order to calculate the salt mass flow rate that maintain the hot and cold tank temperature constant. To this end, the algorithm described in Figure 2.8 is followed. The available HTF hot mass flow and temperature are known from the solar field solver, as well as the cold and hot storage tank temperature.

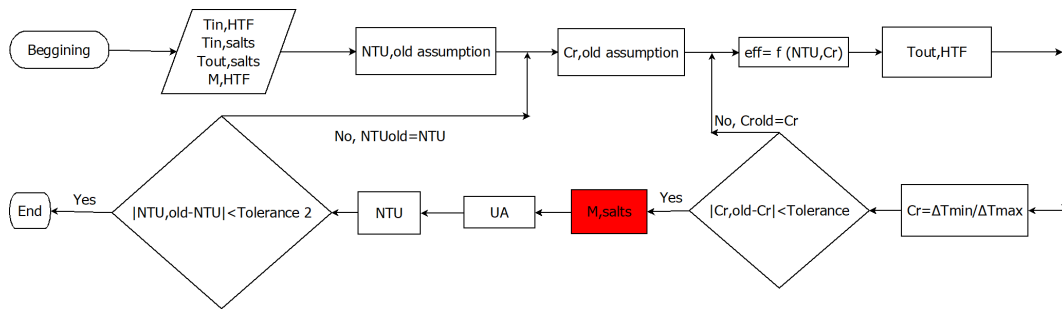


Figure 2.8: Salt mass flow calculation algorithm, own elaboration.

When the storage system is close to being filled it is possible that the available irradiation allows to heat more salt than the remaining empty volume. In this case, the salts mass flow is reduced in order to complete the storage tank volume at the end of the current time step. The reduced salt mass flow is heated without defocusing any collector leading to a higher temperature that generate a slight increase in the hot tank temperature. The new temperature is obtained by solving an energy balance to the hot tank (Equation 2.65). Considering that the increase in the salt mass stored (M_t) in the tank is due to the entrance of heated salts $\dot{m}_{in,s}$ at temperature $T_{in,s}$. The auxiliary variable θ is defined as in 2.67. Finally the expression 2.68 is reached.

$$\frac{d(M_t C_p T_t)}{dt} = \frac{dM_t}{dt} C_p T_t + M_t C_p \frac{dT_t}{dt} = \dot{m}_{in,s} C_p T_{in,s} \quad (2.65)$$

where C_p is the salts specific heat and T_t the tank temperature. Considering

$$\frac{dM_t}{dt} = \dot{m}_{in,s} \quad (2.66)$$

applying the following change of variable

$$\theta = T_t - T_{in,s} \quad (2.67)$$

Equation 2.65 can be re-written as

$$\frac{\partial \theta}{\partial t} = -\frac{\dot{m}_{in,s}}{M_t} \theta$$

once integrated the following expression for θ is reached

$$\theta = \theta_0 e^{-\frac{\dot{m}_{in,s}}{M_t} t}$$

leading to

$$T_t = T_{in,s} + (T_{t,0} - T_{in,s}) e^{-\frac{\dot{m}_{in,s}}{M_t} t} \quad (2.68)$$

2.1.7 System operation

The plant begins to operate when the available irradiation is enough to heat 20% of the nominal HTF mass flow rate. At this condition the heated thermal

fluid is solely employed for generating steam in the power cycle (see Figure 2.9).

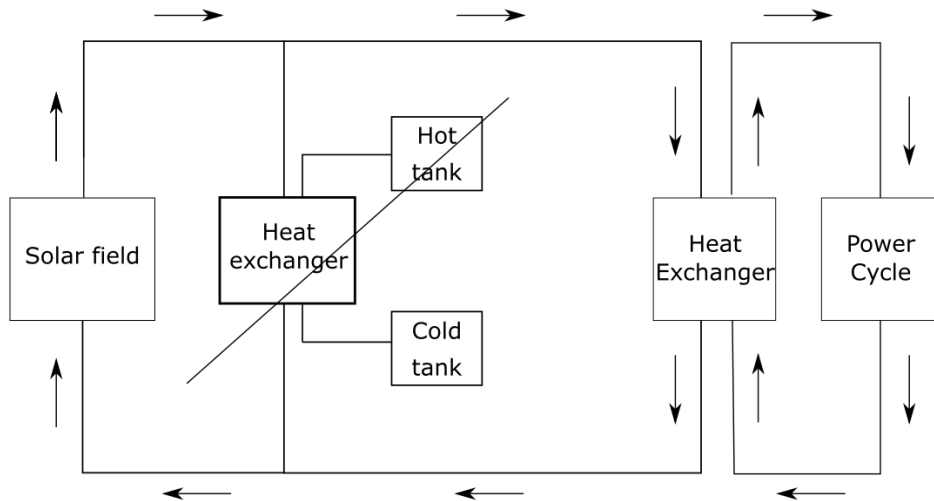


Figure 2.9: Flow configuration, own elaboration.

Since the day continues, the irradiation increases leading to an increase in the heated HTF. At good irradiation conditions the field size allows to heat more HTF than the needed to feed the power cycle, this excess can be employed to heat another fluid (usually molten salts) which is stored. The storage charging process begins when the available incident energy exceeds in 5% the required energy for a nominal functioning of the power cycle (see Figure 2.10).

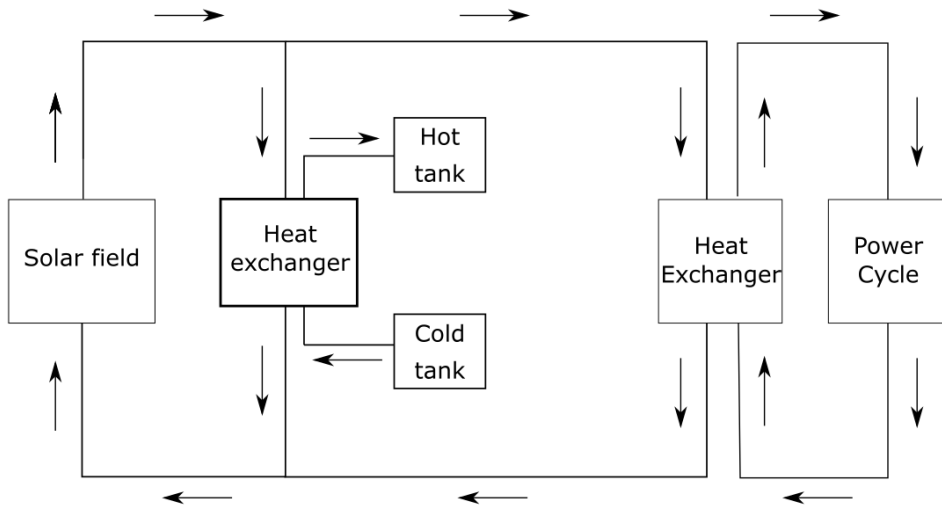


Figure 2.10: Flow configuration when charging storage system, own elaboration.

As irradiation decreases the energy supplied to the power cycle reduces. If the generated steam in the heat exchanger reaches a 90% of the design rate and there is available energy in the storage system, it starts to discharge in order to reach nominal steam conditions. An scheme of this operation mode is presented in Figure 2.11.

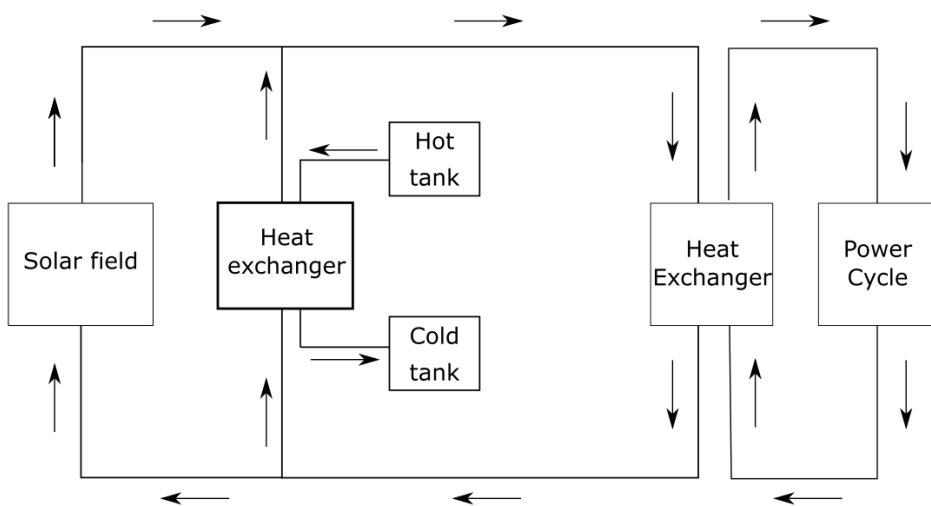


Figure 2.11: Flow configuration when discharging storage system, own elaboration.

If the storage system is filled and the available irradiation exceed the necessary to work at nominal conditions, a fraction of the solar field is defocused

in order to capture only the heat required generate the nominal steam mass flow, leading to a fraction of spilled energy.

2.1.8 Whole plant algorithm

This section intend to explain the way of linking each sub-block explained in previous subsections. The process begins with the solar field solver algorithm where the incident energy is calculated and a first approximation of the HTF mass flow is performed as shown in figure 2.4.

Then the heat exchanger block is solved, where considering the difference between the actual HTF flow to the design one a new HTF cold temperature is calculated. Once this new value is obtained the whole process is repeated until the heat exchanger outlet temperature of two consecutive iterations reach a user-defined uncertainty. Once the process is finished the HTF mass flow rate and temperature decrease in the HTF-steam heat exchanger is known, hence the cycle load can be obtained. Using Figure 2.6 the cycle efficiency is estimated leading to the produced energy (see Figure 2.12). An extra correction factor is applied to calculate the produced energy due to different phenomenons not taken into account being the most relevant presented below:

- Piping heat loss.
- Transient behavior.
- Tracking and pumps power consumption.
- Pipes thermal inertia.

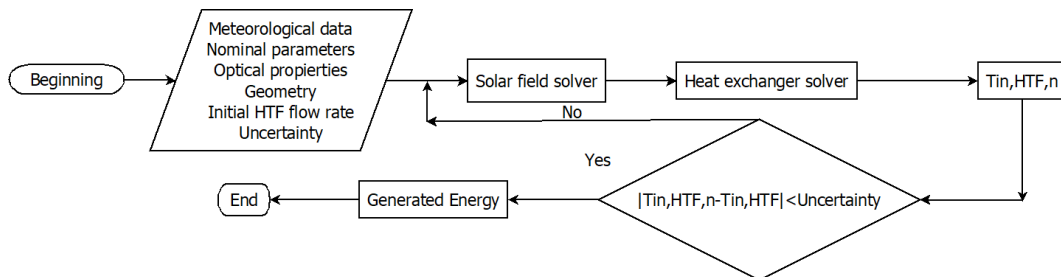


Figure 2.12: Complete solving algorithm, own elaboration

2.2 System Advisor Model

The System Advisor Model (SAM) is a free software, developed by NREL, that allows performance and economic evaluation of several renewable technologies such as photovoltaics, CSP, wind, geothermal, etc. Within CSP technology, SAM can model SPT, PT and LF systems for electric power generation [25].

SAM requires hourly weather data including DNI, ambient temperature, wind speed, ambient pressure and the project location. In addition several financial parameters must be introduced such as the project lifetime, discount rate and the inflation rate. For the economic analysis the system costs must be specified. System Advisor Model count with predetermined values provided by NREL.

SAM's performance models make timestep-by-timestep calculations of a power system's electric output, generating a set of timeseries data that represents the system's electricity production over a single year. The simulation timestep depends on the temporal resolution of the data in the weather file, which can be hourly or subhourly [26].

2.2.1 Solar Power Tower Model

The SPT system design is performed starting from an user specified DNI available at the design point along with the required solar multiple (ratio of the receiver thermal power to the cycle thermal power) and heliostat field multiple. Considering the receiver, the nominal hot and cold HTF temperature at design conditions is required. Finally, storage size, design turbine gross output, estimated gross to net efficiency and power cycle thermal efficiency must be stated.

Considering the specified information, along with geometrical properties of the heliostat (width, height) the Solar Power Tower Model generates the heliostat field layout and characterize its optical performance.

Tower height, receiver dimensions and heat transfer properties are required. For the receiver, a detailed thermal model is employed. This model consists in solving the energy balance in the receiver for each time-step considering multiple heat transfer mechanisms, including incident radiation, external convection and radiation exchange with the surroundings (Figure 2.13).

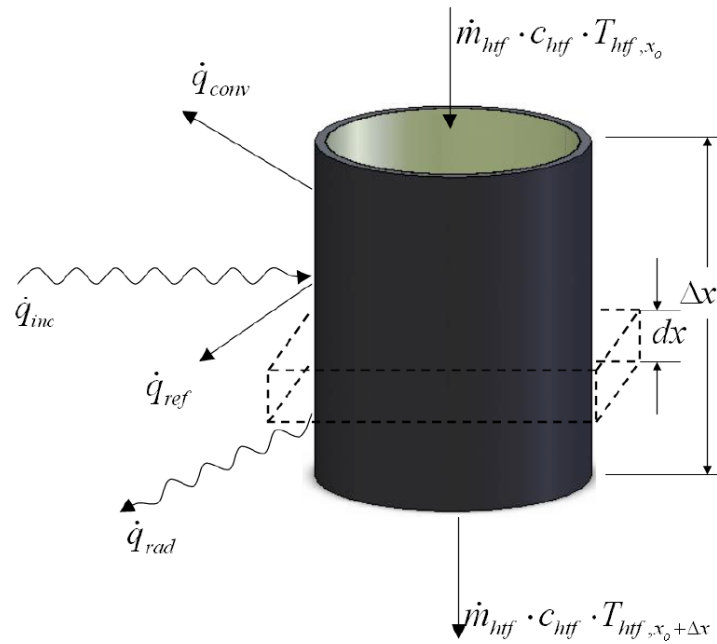


Figure 2.13: Energy balance to receiver [5].

2.2.2 Parabolic Trough Model

For PT, SAM allows two different options for the solar field sizing. The user can define the solar multiple or the solar field aperture. Also several parameters such as row spacing, collector orientation, number of collectors per loop must be specified.

Several collectors mirrors models are available with their correspondent reflective aperture, length, tracking error, reflectance and cleanliness factor (as exposed in Equation 2.11). A receiver library is also available. This library gather geometric and optical information for a wide variety of receivers.

Lastly, the power cycle design gross output, estimated gross to net conversion factor, thermal efficiency and storage size mus be defined. Reference values are available for each field.

The PT model employed by SAM (Figure 2.14) is very similar to the one presented in section 2.1. The main difference on the thermal model rely on the consideration of transient effects (refer to [3] for more information). In addition, the possibility of different power purchase prices during the day is also available.

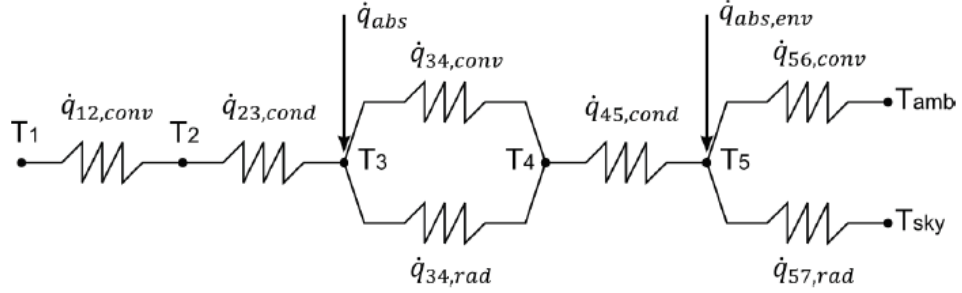


Figure 2.14: Resistance network SAM [3].

2.3 Economic Analysis Procedure

2.3.1 LCOE definition

For energy projects the parameter that should be optimized is the levelized cost of energy (LCOE). This parameter take account the present value of every cost of the project during its lifetime and determines the price of electricity that makes it profitable. A key concept involved in the LCOE calculation is the discount rate (i , interest rate used to determine present value of future cash flows). In this work a typical 8% i value is employed.

A 20 years study period is chosen, equal to the amortization time for the power cycle, solar field, HTF system and balance of plant (BOP). The initial investment is considered to be effected at year 0, when the construction of the plant takes place and no profits are perceived. Due to the lifetime of these technologies no re-investments are considered within the study period. LCOE is determined as described in Equation 2.69.

$$LCOE = \frac{\sum_{a=0}^{b=20} \frac{I_a + M_a}{(1+i)^a}}{\sum_{a=1}^{20} \frac{E_a}{(1+i)^a}} \quad (2.69)$$

where i is the interest rate as defined above, I_a the investment required, M_a the operation and maintenance costs (both fixed and variable), a is each specific year within the 20 years lifetime and E_a the produced energy in the year a . In this work the investment is considered to be executed in the year 0 and no re investments are considered for the study period, in addition no degradation is considered leading to a constant energy production between the different years.

2.3.2 Tax evaluation

For a correct tax evaluation it is important to define the following aspects [27].

Tangible assets: A tangible asset is an asset that has a finite monetary value and usually a physical form. Tangible assets can typically always be transacted for some monetary value though the liquidity of different markets will vary.

Intangible assets: An intangible asset is an asset that is not physical in nature. Goodwill, brand recognition and intellectual property, such as patents, trademarks, and copyrights, are all intangible assets. Intangible assets exist in opposition to tangible assets, which include land, vehicles, equipment, and inventory.

Depreciation: Depreciation is an accounting method of allocating the cost of a tangible or physical asset over its useful life or life expectancy. Depreciation represents how much of an asset's value has been used up. Depreciating assets helps companies earn revenue from an asset while expensing a portion of its cost each year the asset is in use. If not taken into account, it can greatly affect profits.

Amortization: Amortization is an accounting technique used to periodically lower the book value of a loan or intangible asset over a set period of time. In relation to a loan, amortization focuses on spreading out loan payments over time. When applied to an asset, amortization is similar to depreciation.

The tax that apply for these projects in Uruguay (IRAE) represents a 25% of the company utility before taxes, discounting amortizations and depreciation on both, tangible and intangible assets.

In order to foster renewable technology intensive industries several benefits are available, leading to a decrease in the financial costs. These benefits are calculated from the Uruguayan decree 143/018 [28] based on a 1 to 10 punctuation in each area presented in table 2.4 which are afterwards weighted by the factors presented in the same table.

Table 2.4: Weighting factors [28].

Area	Factor
New Jobs	0.40
Exports increase	0.15
Decentralization	0.10
Clean technologies	0.20
I&D+i	0.25
Sector index	0.20
Total	1.30

2.3.3 Procedure

Next the LCOE calculation is explained, using the simulation data. Firstly, the annual generated power is estimated utilizing SAM as explained above. Then an energy price and the annual income is obtained. Production and depreciation costs are deducted leading to the utilities before taxes. IRAE costs are applied along with the corresponding exoneration for each location. Finally, depreciation cost is added since it must be taken into account for tax calculation purposes but not as an actual disbursement.

A LCOE sensitivity analysis is also performed in order to quantify the importance of different aspects of the project. The parameters considered in this analysis are the initial investment costs and produced energy.

Chapter 3

Parameters setting, validation and costs estimation

This chapter present the key aspects for running the simulation, along with the SAM and own code validation. Additionally, the costs that should be considered in the economic procedure are discussed.

3.1 Simulation implementation

There are several factors that affect the results and thus must be clearly defined. The parameters detailed in this sections are kept constant throughout the simulations. For Parabolic Trough technology the parameters presented in this section are used for both, own code and SAM simulations. On the other hand the data presented for Solar Power Tower refer to the input data for a cylindrical receiver requested by the mentioned software.

For radiation data, ambient temperature, wind speed and other relevant meteorological data the Typical meteorological year (TMY) developed by LES for the mentioned five different locations are employed [13].

3.1.1 Parabolic trough

Considering a typical parabolic trough power plant the following nominal parameters are defined for the study case:

- HTF solar field inlet temperature (T_{in}): $293^{\circ}C$
- HTF solar field outlet temperature (T_{out}): $393^{\circ}C$

- Storage tank cold temperature ($T_{c,s}$): $290^{\circ}C$
- Storage tank hot temperature ($T_{h,s}$): $386^{\circ}C$
- Turbine inlet pressure: 100 bar
- Inlet steam generator temperature ($T_{sg,in}$): $230^{\circ}C$
- Outlet steam generator temperature ($T_{sg,out}$): $370^{\circ}C$
- Deviation in the receiver tube position from the optical focus (γ_{int}): 0.95
- Collector: SkyFUEl SkyTrough (with 70-mm receiver)
- Reflective aperture area: $865.5 m^2$
- Aperture width, total structure: $6.07m^2$
- Length of collector assembly: $150m$
- Number of modules per assembly: 12
- Average surface-to-focus path length: $2.15 m$
- Mirror reflectivity (ρ_{mirror}): 0.935
- Receiver: Schott PTR70
- Absorber tube inner diameter: $0.066m$
- Absorber tube outer diameter: $0.07m$
- Glass envelope inner diameter: $0.119m$
- Glass envelope outer diameter: $0.125m$
- Glass transmissivity (τ_{glass}): 0.96
- Glass absorptivity (α_{glass}): 0.02
- Glass emittance: 0.86
- Receiver absorptivity ($\alpha_{receiver}$): 0.96
- Cleanliness factor (cf): 0.98
- Air cooled condenser

The geometry (reflective aperture area, aperture width, length of collector assembly, etc) was selected as in SOLIDA [18]. The rest of the parameters were setted considering SAM [25] typical values.

As thermal fluid Therminol VP-1 is considered, SAM automatically calculates the needed properties. Regarding the own code elaborated, the free software OCTAVE is employed as simulation software due to its simplicity. The HTF properties considered in this code are obtained as function of the

temperature as follows [29]:

$$\rho \left[\frac{kg}{m^3} \right] = -0.90797T(^{\circ}C) + 0.00078116T^2(^{\circ}C) - 2.367x10^{-6}T^3(^{\circ}C) + 1083.25 \quad (3.1)$$

$$C_p \left[\frac{kJ}{kgk} \right] = 0.002414T(^{\circ}C) + 5.959x10^{-6}T^2(^{\circ}C) - 2.9879x10^{-8}T^3(^{\circ}C) + 4.4172x10^{-11}T^4(^{\circ}C) + 1.498 \quad (3.2)$$

$$k \left[\frac{W}{mK} \right] = -8.19477x10^{-5}T(^{\circ}C) - 1.92257x10^{-7}T^2(^{\circ}C) + 2.5037x10^{-11}T^3(^{\circ}C) - 7.2974x10^{-15}T^4(^{\circ}C) + 0.137743 \quad (3.3)$$

$$\nu \left[\frac{mm^2}{s} \right] = exp \left(\frac{544.149}{T(^{\circ}C) + 114.43} - 2.59578 \right) \quad (3.4)$$

3.1.2 Solar Power Tower

The parameters setted for the SPT technology are presented below. The heliostat area was selected as in SOLIDA [18] while the other parameters are setted to typical SAM [25] values.

- HTF hot temperature (T_{hot}): $565.6^{\circ}C$
- HTF cold temperature (T_{cold}): $287.8^{\circ}C$
- Design turbine net output: 110 MW
- Turbine inlet pressure: 100 bar
- Cycle thermal nominal estimated efficiency: 0.439
- Heliostat area: $66.1m^2$
- Tower height: 180 m
- Receiver height: 21.6m
- Mirror reflectivity and soiling factor: 0.9135
- Mirror availability factor: 1
- Mirror ratio of reflective area: 1 (the fraction of the area defined by the heliostat width and height that actually reflects sunlight)
- Heliostat stow/deploy angle: 8 degrees
- Wind stow speed: $15 \frac{m}{s}$
- Air cooled condenser

3.2 Validation

In order to carry on, the SAM advisor power tower and parabolic through model, along with the own code generated are validated against the results exposed by Solida [18]. In the mentioned work, six configurations (solar field and storage size) are analyzed for each technology. Since Solida [18] was developed in 2014, an older version of the TMY (1.0) was employed. In order to minimize the uncertainties, the same TMY version was employed during the validation.

3.2.1 Solar Power tower

In this section the different every solar field sizes and storage size configurations presented in SOLIDA [18] are considered in order to reach an accurate validation. This comparison is presented in Table 3.1 where results are expressed in generated electricity energy (*GWhe*, different from thermal energy).

Table 3.1: System Advisor Model Validation, own elaboration.

Solar Power Tower 110 MW			
Number of heliostats/ Storage hours	GWhe SOLIDA	GWhe SAM	Deviation (%)
16770/5	320.8	320.6	-0.062
18295/5	328.2	329.1	0.274
18295/7.5	364.9	361.3	-0.996
19819/7.5	373.2	373.7	0.134
19819/10	398.6	398.2	0.100
21343/10	408.8	410.7	0.465

Great similarity between both models results is observed, leading to a maximum output tower difference of 1%, an MBD error of 0.04% and a RMSD of 0.47% (see Figure 3.1). This results reaffirms that SAM is a good choice for the simulation software.

3.2.2 Parabolic Trough

The parabolic trough validation includes not only the results obtained using SAM but also the own code verification (Table 3.2) both compared to the results obtained in Solida [18] for every configuration presented in the mentioned work

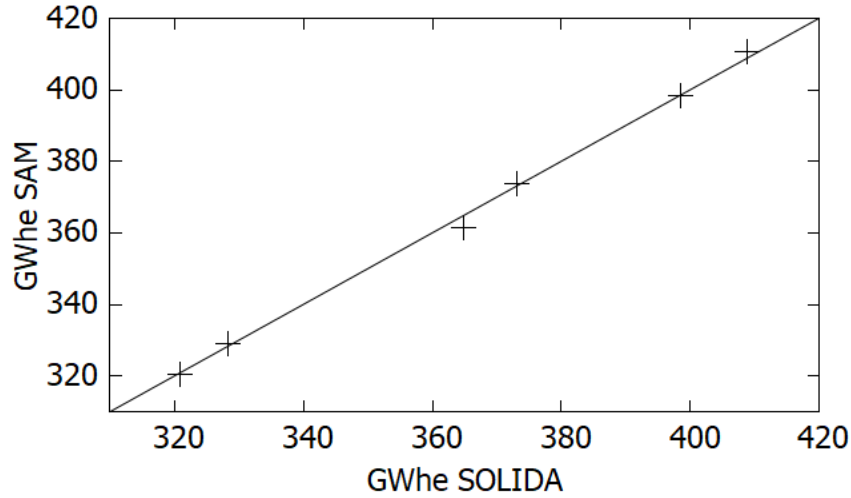


Figure 3.1: Solar power tower SAM vs Solida predictions

Table 3.2: System Advisor model and own code validation against Solida [18], own elaboration.

Parabolic Trough 55MW					
N ^o Loops/ Storage hours	GWhe SOLIDA	GWhe SAM	SAM Deviation (%)	GWhe Own Code	Own Code Deviation (%)
92/0	84.2	85.9	-2.0	85.3	-1.3
123/0	99.0	97.2	1.9	100.9	-1.9
123/5	123.5	126.0	-2.0	125.0	-1.2
155/5	143.2	144.4	-0.8	143.0	0.1
155/7.5	152.5	156.0	-2.3	154.0	-1.0
186/7.5	168.0	172.0	-2.4	168.7	-0.4

When analyzing the results, great accordance between both codes to SOLIDA [18] is observed. In no configuration the difference between the predicted generated energy surpass 2.5% what seems a reasonable margin. It is also observed that both codes tend to overestimate the produced energy (compared to SOLIDA [18]). For SAM, MBD and RMSD errors are -1.44% and 2.0% . On the other hand the developed code MBD and RMSD are -0.84% and 1.0% (see Figure 3.2). Since SAM is widely used by scientific community, more phenomenons are taken into account and the simulation duration is considerably lower, this tool is chosen for the CSP simulations.

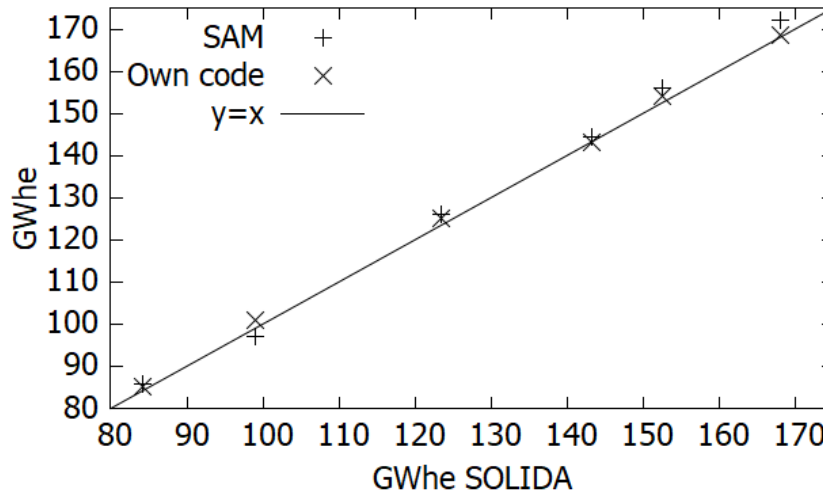


Figure 3.2: Parabolic trough SAM and own code vs Solida predictions

3.3 Costs

3.3.1 Initial Investment

A key aspect for performing a good analysis is to accurately determine the cost involved in the development of these projects. An extensive literature review was performed, leading to different initial investment costs which are presented in Annex B discriminated by installed capacity and technology. Other relevant aspects such as the project location, available irradiation in the considered zone and storage size are also specified.

As presented in Annex B in Tables B.1 to B.6 , detailed information is mainly available for projects located in China, leading to initial investment costs of around $5.0 \frac{MUSD}{MW}$ for 110 MW Solar Power Tower with 10 or more storage hours and $6.0 \frac{MUSD}{MW}$ for 55 MW Parabolic plants at the same storage conditions.

A considerable difference is appreciated when comparing to projects located elsewhere (Tables B.7 and B.8 for USA and Spain respectively in Annex B). Although this difference may be influenced by the technology learning curve (since papers for projects located in China tend to be newer) it seems the difference is too large to be only explained by this factor.

Another relevant source of information is the available economic data for System Advisor Model by (NREL). NREL provides detailed information specifying costs for every component of the plant, in particular solar field and

storage size. These costs are considered during the optimization, leading to $145 \frac{USD}{m^2}$ and $24 \frac{USD}{MWh}$ costs for solar field and storage respectively for SPT technology and $150 \frac{USD}{m^2}$ and $65 \frac{USD}{MWh}$ for the PT case (See Tables B.9 and B.10 in Annex B).

In order to compare this information to the one presented in Tables B.1 to B.6, 23335 heliostats and 254 loops power tower and parabolic trough plants are considered, both with a 12.5 hours storage system.

When comparing the results obtained considering NREL information, of $6.0 \frac{MUSD}{MW}$ and $7.9 \frac{MUSD}{MW}$ for 110 MW solar power tower and 55 MW Parabolic Trough respectively, to the initial costs obtained from the mentioned papers of $5.0 \frac{MUSD}{MW}$ and $6.0 \frac{MUSD}{MW}$ a great difference is observed. Due to this factor, two different scenarios are considered for the economic analysis varying the initial investment cost between the values presented.

The obtained I.I. cost are compared to the ones exposed in [30]. Figure 3.3 shows the evolution of initial investment cost differentiated by technology and storage capacity. At the end of 2019, the values obtained in this study are placed. It is observed that the worst scenario for PT technology and the first years PT power plants present a similar behavior, while the most favorable case is comparable to the last plants installed. Regarding SPT technology, no information is available before 2014. This can be explained since this technology great development take place in the last years. However both scenarios look reasonable, although the favorable scenario seem to suit better the 2018 and 2019 tendency. Finally the investment costs employed in SOLIDA [18] are presented. The initial investment cost for the optimal SPT and PT power plant with 10 hours and 7.5 hours storage sizes respectively ascend to $6.2 \frac{MUSD}{MW}$ and $5.8 \frac{MUSD}{MW}$, considering an Euro-Dolar exchange rate of 1.3.

3.3.2 Operation and maintenance

In this work the operation and maintenance (*O&M*) costs available in SAM ([25]) are employed ¹. For both technologies, $66 \frac{USD}{kW-year}$ fixed *O&M* are considered. The SPT and PT variable *O&M* costs ascend to $3.5 \frac{USD}{MWh}$ and $4.0 \frac{USD}{MWh}$ respectively.

¹these OPEX costs are valid for the US, there might be differences when adapting to the uruguayan context



Figure 3.3: Initial Investment Costs Figure obtained from [30] modified to show this work prediction in black (year 2020)

3.3.3 Taxes

As presented in Table 2.4 in section 2.3.2 the factors that must be taken into account for calculating the tax exoneration in renewable energy projects are new jobs generated, exports increase, decentralization, clean technology, $I&D + i$ and a sector index.

Due to the lack of information to perform an accurate estimation of the jobs generated and the assumption that this factor will not be significant, no punctuation in this item is assigned, as in the exports increase area. Therefore, the maximum punctuation is assigned in clean technologies, $I&D + i$ and sector index (Vanguard Renewable energy sector). Lastly, the decentralization factor depends on the location of the project, differentiating between departments and the location within it (cities or rural). The appropriate value for each department considered is presented in table 3.3.

Table 3.3: Decentralization punctuation [28].

Location	Decentralization punctuation
Salto	10
Rivera	10
Montevideo	6
Colonia	8
Rocha	8

Finally, the total punctuation for each location is presented in Table 3.4 along with the exoneration capacity (as a percentage of the initial investment) and exoneration duration. It must be stated that the exonerated tax is topped up by an 80% of the corresponding IRAE. Both, exoneration capacity and duration are calculated from the industrial sector simulator, available in the website of Ministerio de Economía [31].

Table 3.4: Final tax exoneration.

Location	Total punctuation	Exoneration (%)	Exoneration period
Salto	7.5	80	20
Rivera	7.5	80	20
Montevideo	7.1	80	19
Colonia	7.3	80	20
Rocha	7.3	80	20

Chapter 4

Optimization and results

In the current chapter, solar field and storage size are optimized in order to reach the minimum possible LCOE. Optimal configurations for each technology and location are presented along with its achieved LCOE for both cost scenarios mentioned above. In addition a comparison to the results obtained by SOLIDA [18] is performed in order to analyze the impact of the optimization.

A sensitivity analysis is presented to visualize the impact of the initial investment costs and generated electricity in the final result. Lastly, annual electricity generation considering both technologies and every location are exposed.

4.1 Optimization

The optimization consists in finding the storage and solar field size that minimizes the LCOE value. This process is implemented for both technologies and every location where irradiation data is available, Figures 4.1 and 4.2 shows LCOE evolution for the worst costs case scenario as a function of the mentioned parameters for a Power Tower and Parabolic Trough plants respectively, located in Salto.

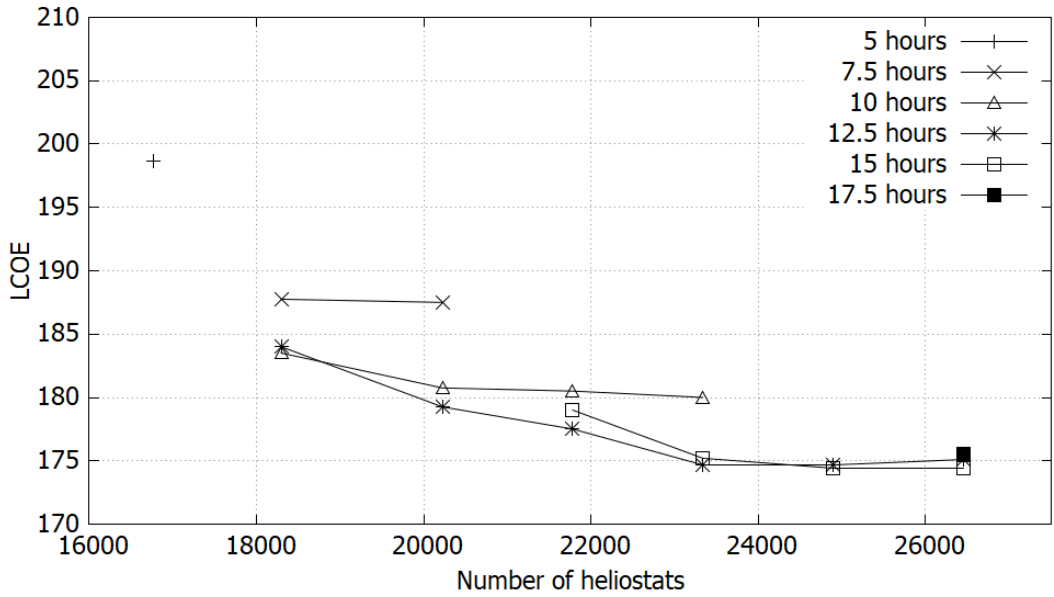


Figure 4.1: LCOE optimization Power Tower Salto study case, heliostat area $66.1m^2$. Own elaboration utilizing SAM.

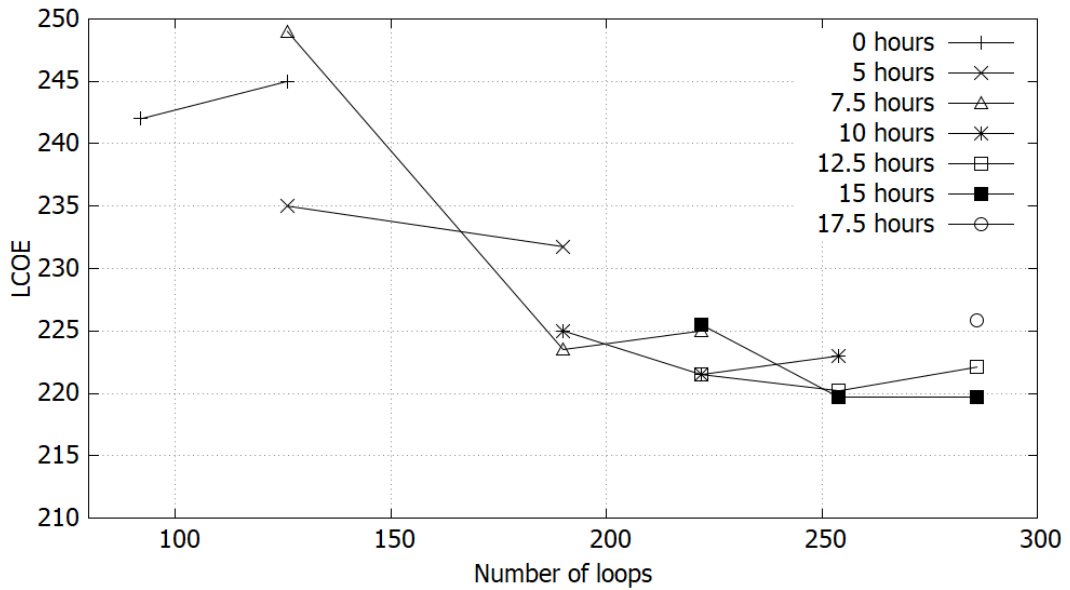


Figure 4.2: LCOE optimization Parabolic Trough Salto study case, loop area $3462m^2$. Own elaboration utilizing SAM.

As presented in Figures 4.1 and 4.2, LCOE reaches rather constants values for storage sizes of 12.5 to 17.5 hours and large solar fields. When this behavior is reached, the criteria adopted is to opt for the less capital demanding option (smaller solar field and storage size). The optimal configuration for each considered location is presented in tables 4.1 and 4.2.

Table 4.1: Solar Power Tower optimal configuration and LCOE, own elaboration utilizing SAM.

Location	Number of heliostats	Storage size (hours)	LCOE (USD/MWh)
Salto	23335	12.5	174.7
Colonia	24891	12.5	176.0
Montevideo	23335	12.5	181.8
Rivera	24891	15.0	184.3
Rocha	24891	15.0	194.7

Table 4.2: Parabolic Trough optimal configuration and LCOE, own elaboration utilizing SAM.

Location	Number of loops	Storage size (hours)	LCOE (USD/MWh)
Salto	254	12.5	220.0
Colonia	254	12.5	220.9
Montevideo	254	12.5	227.3
Rivera	286	15.0	236.1
Rocha	254	12.5	243.7

The same analysis considering the initial investment costs stated in study cases for China is presented in Table 4.3 for Salto location.

Table 4.3: LCOE calculation considering favorable investment conditions for Salto.

Technology	I.I. (MUSD/MWh)	I.I. Variation (%)	LCOE (USD/MWh)	LCOE variation (%)
Power Tower	5.0	-16.7	148.4	-15.0
Parabolic Trough	6.0	-24.0	168.8	-23.3

Great difference between the proposed scenarios is observed. In no case this technology proves to be competitive to photovoltaic or wind projects power plants. However considering the favorable scenario the obtained electricity costs are comparable to fossil fuels plants such as "Punta del Tigre" working with gas oil as fuel (around $147 \frac{USD}{MWh}$).

Lastly, a comparison of the obtained results for both scenarios and technologies against those exposed in Figure 1.11 is presented in Figure 4.3. It is observed that the results for both technologies (SPT in blue and PT in red) tend to be lower to any region, excepting China.

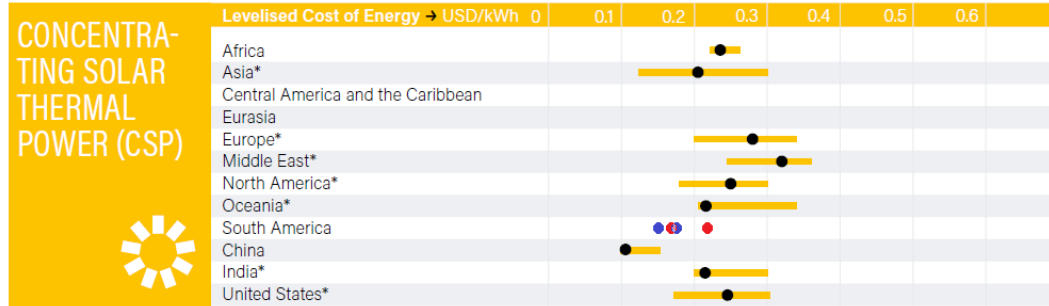


Figure 4.3: Levelized cost of energy in different locations including obtained results for both scenarios (SPT in blue, PT in red), modified from [9].

4.2 Comparison against results obtained by SOLIDA

Once the optimal configuration is determined, a inflationary 2% component for OPEX costs ¹ and 0.2% electricity generation degradation are considered in order to compare the obtained results to the ones presented in SOLIDA [18]. Another factor that must be considered for a correct comparison is extending the amortization and economic analysis to 25 years as employed in the mentioned paper. Some of the benefits calculated (IRAE exoneration) only apply for the first 20 years. The obtained result for LCOE and its comparative is presented in Table 4.4 for both technologies located in Salto.

Regarding the initial investment cost employed the NREL scenario is considered since in the year of publication of the previous work no China projects where implemented or studied. Considering the SPT technology, SOLIDA [18] and NREL costs are similar ($6.2 \frac{MUSD}{MW}$ and $6.0 \frac{MUSD}{MW}$, respectively) although the storage sizes differ (10 hours in SOLIDA [18] and 12.5 for the NREL study case). For PT the scenario is quite different $5.8 \frac{MUSD}{MW}$ in SOLIDA against $7.9 \frac{MUSD}{MW}$ in the present study. This can be explained by an important storage size difference (7.5 hours in SOLIDA [18] vs 12.5 hours in the current study case).

¹Operating expense cost

Table 4.4: LCOE ($\frac{USD}{MWh}$) comparison salto study-case. Adapted LCOE considers electricity generation degradation and inflationary effects

Previous LCOE	LCOE Adapted	LCOE 25 years	LCOE SOLIDA [18]	LCOE variation (%)
Power Tower				
174.7	180.3	171.0	190.3	-11.3
Parabolic Trough				
220.0	226.4	213.9	243.5	-13.8

Although there are some uncertainties regarding the initial investment, results show an important decrease regarding the LCOE presented in SOLIDA [18]. This shows the optimization achieved for the solar field and storage size, combined with a new cost evaluation result favorable leading to an LCOE reduction over 10%.

4.3 Sensitivity

A sensitivity analysis is performed considering 5% variations in the initial investment cost and generated energy, the results are presented in Table 4.5.

Table 4.5: LCOE sensitivity for Salto optimal study case, own elaboration utilizing SAM.

Variation	Initial Case	Initial investment		Generated energy	
		+5%	-5%	+5%	-5%
LCOE Power Tower	174.7	182.6	167.7	166.5	183.7
LCOE Parabolic Trogh	220.4	230.5	209.9	209.9	231.5
LCOE power tower variation (%)	-	4.5	-4.0	-4.7	5.2
LCOE parabolic trough variation (%)	-	4.6	-4.7	-4.7	5.0

It is observed that each variation generate a similar behavior in the resulting LCOE, this phenomenon can be explained by the great influence of these factors relegating other considerations (OPEX costs, taxes, etc.) to a second plane.

4.4 Energy

In National Energetic Balance [11] it is stated that Uruguay’s final electricity consumption ascends to 973.1ktep equivalent to 11.32TWh. Table 4.6 show the electricity generation prediction for Solar Power Tower and Parabolic Trough technologies in every location considered for the optimal configuration obtained in each case.

Table 4.6: Annual electricity generation, own elaboration utilizing SAM.

Location	110 MW SPT		55 MW PT	
	Annual Electricity Generated (GWh)	Capacity Factor (%)	Annual Electricity Generated (GWh)	Capacity Factor (%)
Salto	442.5	45.9	229.0	47.5
Colonia	450.8	46.8	227.8	47.3
Montevideo	425.2	44.1	221.7	46.0
Rivera	439.5	45.6	238.4	49.5
Rocha	415.7	43.1	206.1	42.8

¹Note that configuration may vary between locations as presented in Tables 4.1 and 4.2.

Considering the results for Salto, the obtainable energy with the optimal configurations reach 3.9% and 2.0% of the yearly total electricity demand. This great amount of electricity generation for a solar project can be explained by the storage sizes considered that allows the plant to be working even at night. The impact of the storage is also observed in the capacity factors obtained (between 40% and 50%), much higher than other solar technologies such as photovoltaics (around 18%).

To a better understanding of this phenomenon, daily mean evolution of DNI (Figure 4.4) and gross power cycle generated power are presented for the months of January and July, considering Salto location.

Figure 4.5 shows that studied SPT case in January can provide energy through all the day. During July there several hours of no generation are observed. PT technology presents a similar behavior (see Figure 4.6).

In the current work no incentives for selling electricity at peak hours (namely from five in the afternoon until eleven at night) is considered. Future works can explore the impact of considering different prices according the demand existent in the electric grid, maximizing the advantages of counting with a storage system.

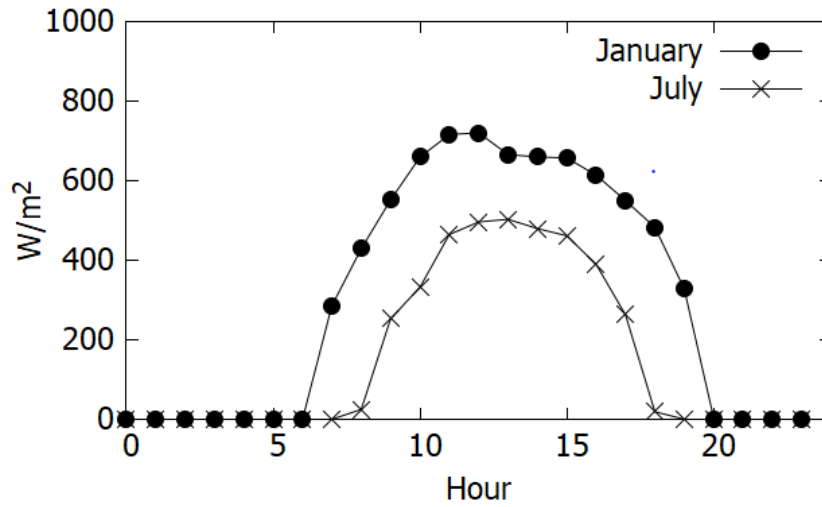


Figure 4.4: Salto January and July mean DNI, own elaboration utilizing SAM.

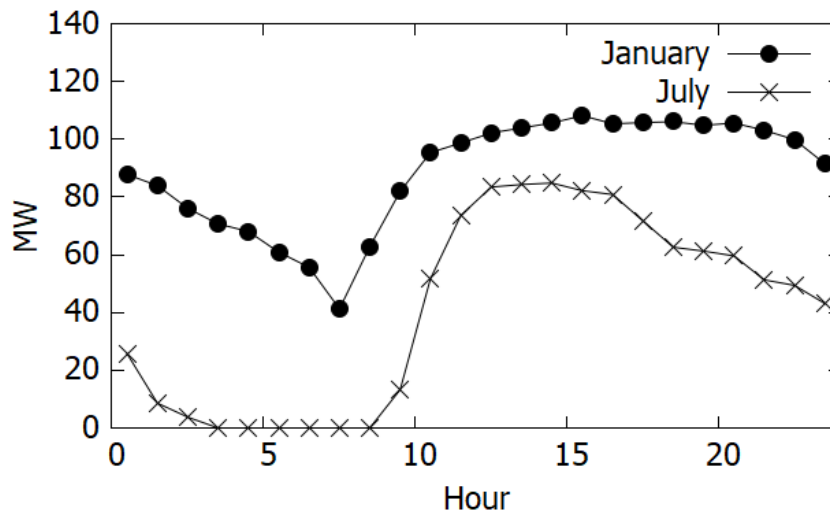


Figure 4.5: SPT mean January and July generation for Salto optimal study case, own elaboration utilizing SAM.

The evolution of the energy generation during the year is now exposed. Figure 4.7 shows that the predicted electricity generation for SPT technology during January, November and December nearly doubles the one prognosticated during winter months (May, June, July). A similar effect is visualized for PT technologies (see Figure 4.8).

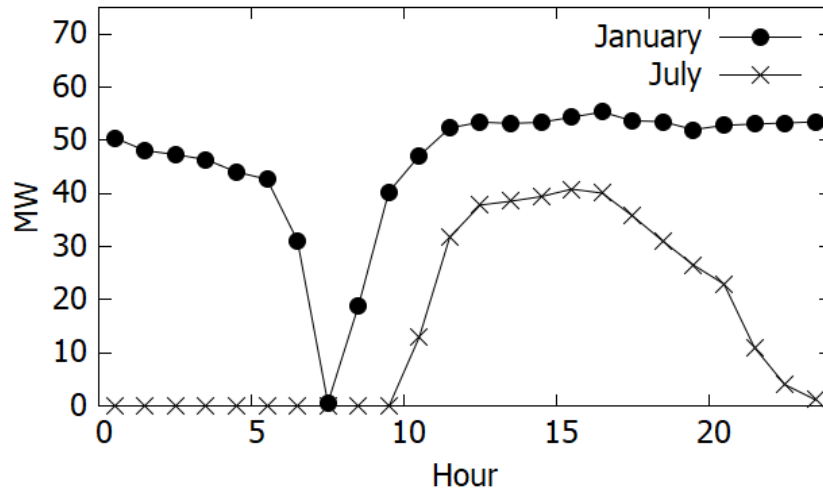


Figure 4.6: PT mean January and July generation for Salto optimal study case, own elaboration utilizing SAM.

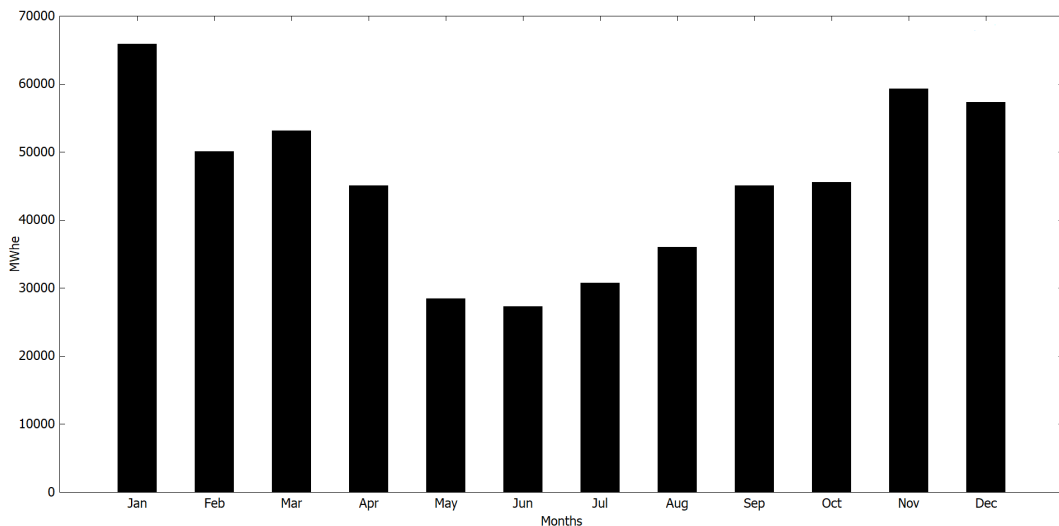


Figure 4.7: SPT monthly generation prediction for Salto optimal study case, own elaboration utilizing SAM.

For the SPT and PT study case the electricity obtained in January ascends to $65.9GWh$ and $34.4GWh$ respectively significantly higher than the $30.7GWh$ and $11.6GWh$ predicted generation for July.

For a better understanding of both technologies, the importance of the different losses is evaluated (see Figures 4.9 and 4.10). Firstly the optical efficiency is calculated as the fraction of energy reaching the receiver over the incident energy in the mirrors. After reaching the receiver, part of the energy is transferred to the HTF while another fraction is lost to the ambient (receiver losses). The heated HTF is directed towards the heat exchanger where the

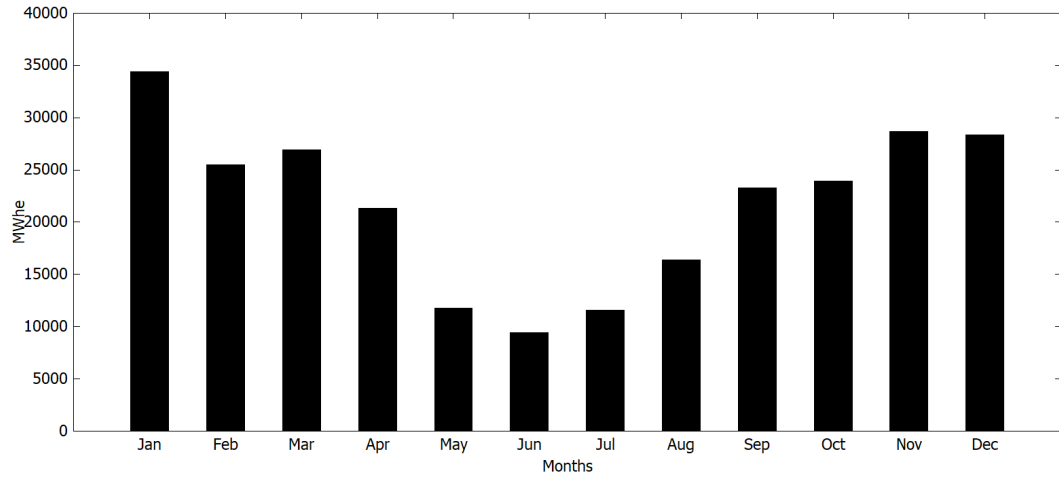


Figure 4.8: PT monthly generation prediction for Salto optimal study case, own elaboration utilizing SAM.

steam is generated, leading to piping and heat exchangers losses. Finally the rankine cycle losses and parasitics (such as water pumps) must be considered.

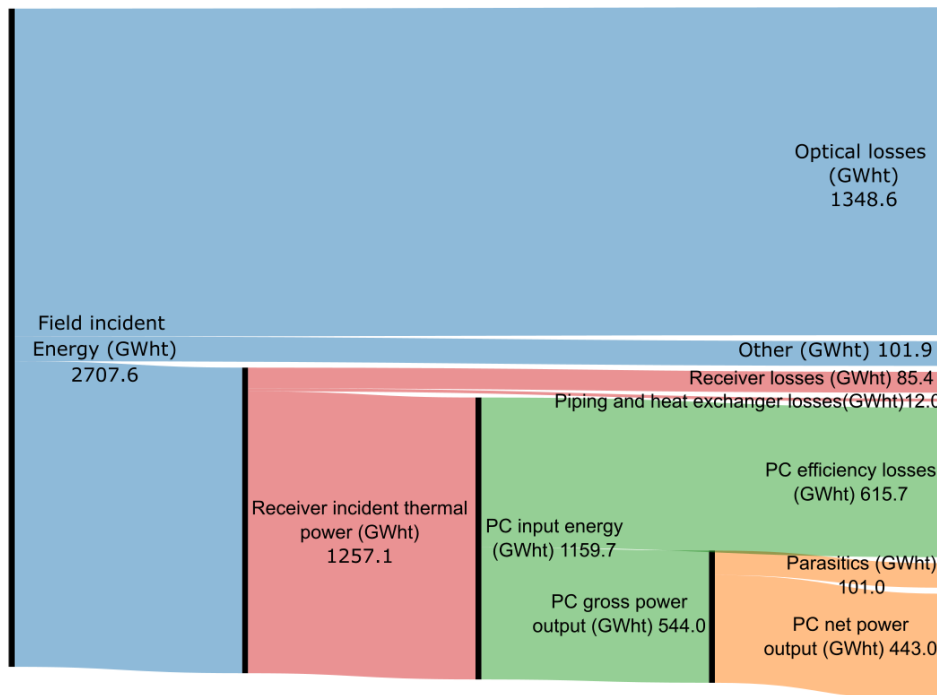


Figure 4.9: SPT losses for Salto optimal study case, own elaboration utilizing [32].

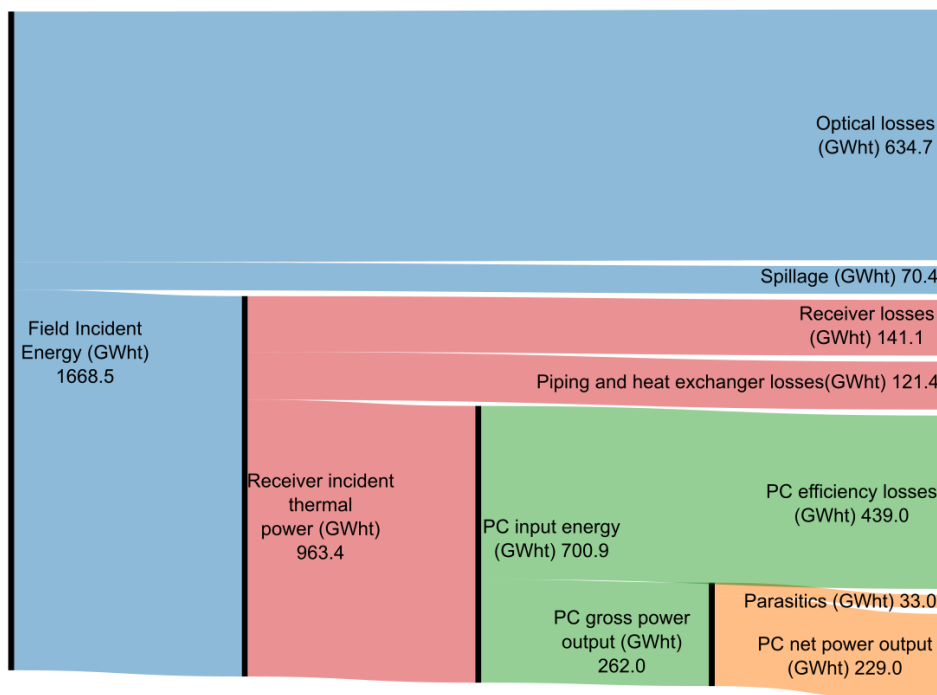


Figure 4.10: PT losses for Salto optimal study case, own elaboration utilizing [32].

In both cases the optical losses prevail, being more relevant in the SPT technology, around 50% of the total field incident energy, against 38% in the PT plant. A great difference in the importance of receiver, piping and heat exchangers losses can be observed (3.6% of total incident energy for SPT and 15.7% for PT). This can be explained since SPT technology employs an unique point receiver, while PT employs line receivers attached to each mirror, increasing the heat transfer area. The second higher source of losses takes place in the power cycle (PC in Figures 4.9 and 4.10) where around 20% and 26% of the field incident thermal power is lost (corresponding to 38.2 power cycle efficiency for SPT and 32.7% for PT).

Figures 4.11 and 4.12 show the hourly evolution of the mean optical efficiency for the months of January and July.

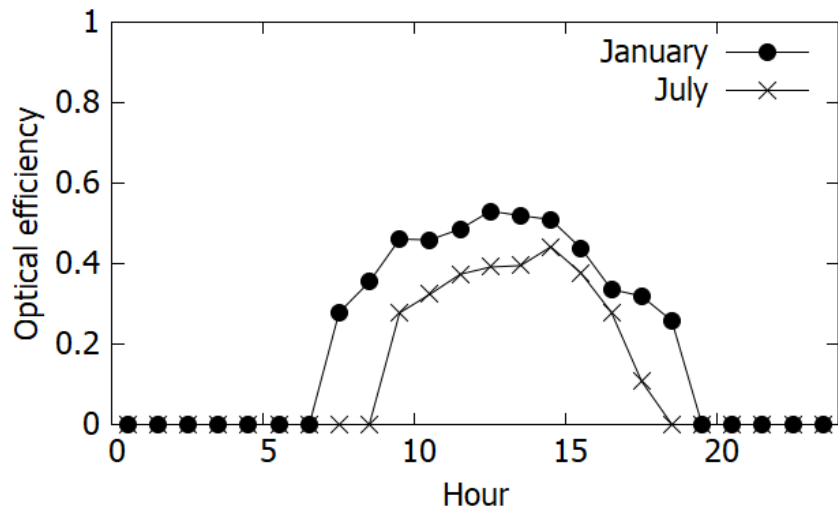


Figure 4.11: SPT optical efficiency Salto study case, own elaboration utilizing SAM.

According to M. Wagner [5] in SPT “The first and most significant loss to be discussed is attenuation due to the angle between the incident solar beam radiation and a vector normal to the surface of the heliostat. This is called the cosine effect, since the radiation reflected to the receiver by the heliostat mirror is proportional to the cosine of the angle in question.”. Less significant optical losses can be explained by shading, atmospheric attenuation, maintenance and errors in tracking.

Figure 4.13 presents a qualitative scheme of the cosine effect variation for a given solar position in the northern hemisphere.

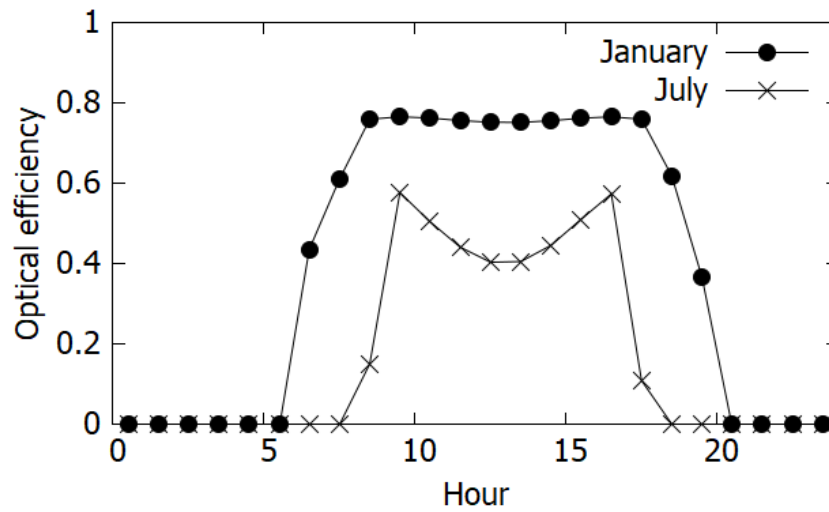


Figure 4.12: PT optical efficiency Salto study case, own elaboration utilizing SAM.

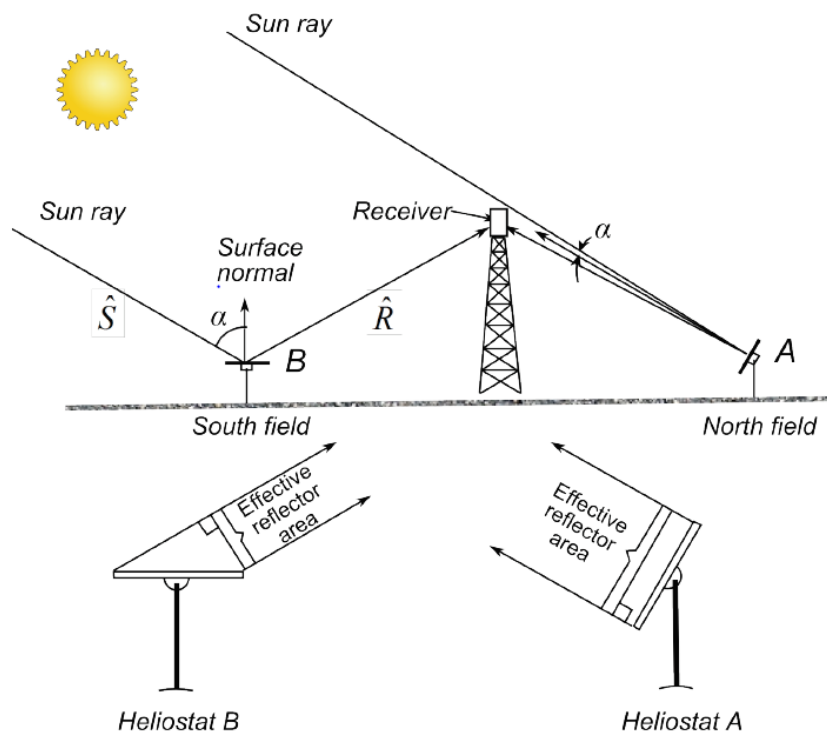


Figure 4.13: Cosine effect. Source [5].

In the southern hemisphere the heliostats present less cosine losses when placed south from the tower, however due to the large solar field sizes to place all the heliostats as mentioned is not reasonable since the distance to the receiver increases. A typical configuration can be observed in Figure 1.5 where mirrors are placed all around the receiver but with a prevailing direction.

Figure 4.14 presents the sun relative position of the mirrors at noon in summer, indicated in black, while the mirrors indicated in sky blue represent the position at noon for winter. No great difference is expected in the optical efficiency of the mirrors placed southerly, however a great increase is observed in the incidence angle of the heliostats placed to the north of the tower, decreasing the optical efficiency of the solar field.

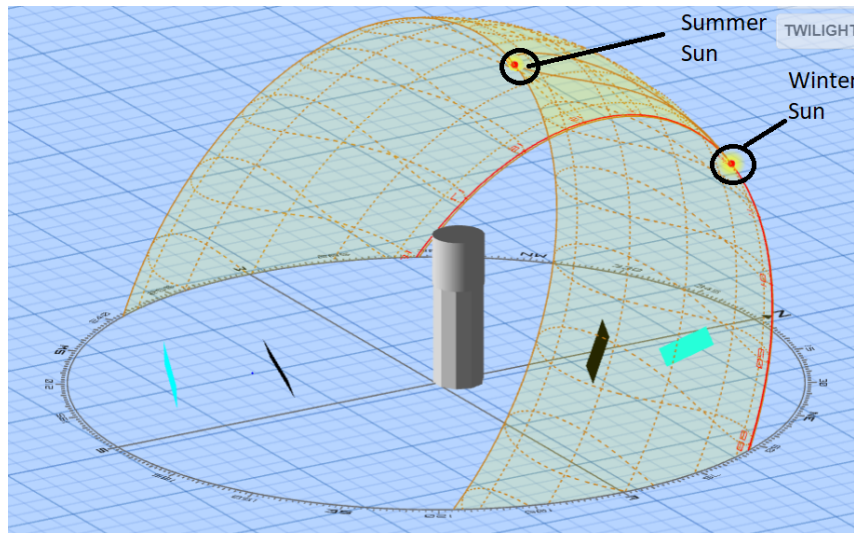


Figure 4.14: Noon summer (black heliostats) and winter (sky blue heliostats) configuration , own elaboration utilizing [33].

Figure 4.12 also shows a significant decrease in optical efficiency for PT technologies. Similarly to SPT, this can be explained by the increase in the incidence angle during winter months (see Figure 4.15)

Finally the location effect is analyzed by simulating the optimal Salto configuration in the different locations where the TMY is available. The annual energy generated and optical efficiency are presented in Table 4.7 for every location.

In the uruguayan case, the optical efficiency behavior turns out to be independent of the location. Furthermore, Figure 4.16a and 4.16b show a linear approximation of the annual energy produced against DNI for SPT and PT technologies, obtaining $R_{SPT}^2 = 0.92$ and $R_{PT}^2 = 0.99$. This results are limited to low geographical variations (see Table 1.3).

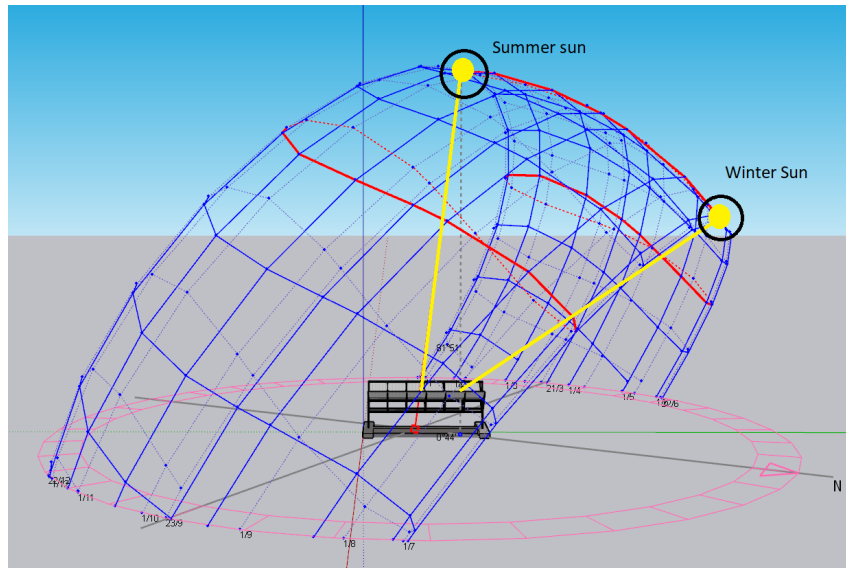


Figure 4.15: Noon summer and sun location , own elaboration using sketchup.

Table 4.7: Location effect, own elaboration utilizing SAM.

Location	Irradiance (kWh/m ² year)	110 MW SPT		55 MW PT	
		Annual Energy GWhe	Optical efficiency (%)	Annual Energy GWhe	Optical efficiency (%)
Salto	1897.5	442.5	50.0	229.0	62.0
Colonia	1890.3	437.5	50.0	227.8	60.2
Montevideo	1862.5	425.2	49.6	221.7	61.0
Rivera	1779.7	417.1	50.8	212.3	60.0
Rocha	1740.6	394.0	50.0	206.1	60.0

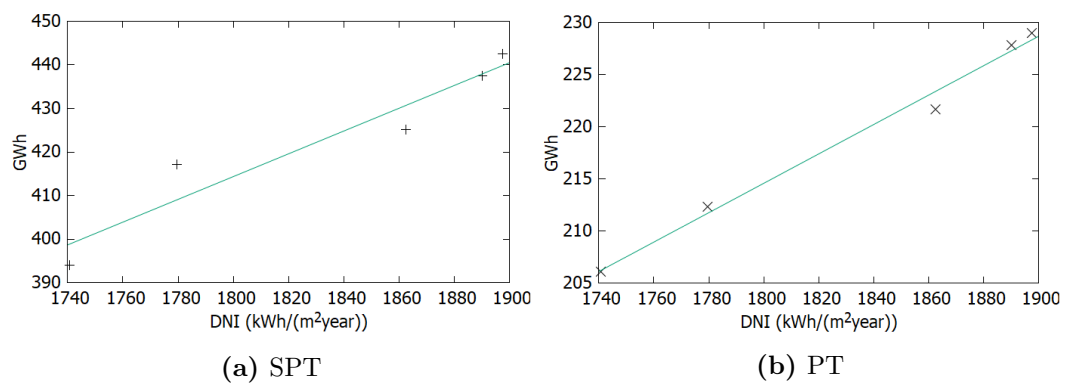


Figure 4.16: Annual energy generated as function of the available irradiance, own elaboration utilizing SAM.

Chapter 5

Conclusions

Concentrating Solar Power (CSP) technologies are getting increasing consideration from researchers and countries all around the world, since they represent a renewable alternative for power or heat production that, unlike wind and photovoltaic technologies, can easily incorporate thermal storage.

The attention these technologies are catching is leading to an important decrease on initial investment costs and an increase of capacity factors making the technology more competitive.

The current work focuses on the optimization of the solar plant configuration in different locations situated in Uruguay. Solar Power Tower (SPT) and Parabolic Trough (PT) technologies are considered due to their higher development for electricity projects around the world.

For PT technology a physics-based own code, that models heat transfer phenomena in the solar field, storage system and heat exchangers was successfully developed. The mentioned code is validated against a previous work developed for Uruguay [18] and System Advisor Model (SAM [25]). Great accordance is observed, leading to a maximum variation of 2% in the annual produced energy.

In order to execute an adequate economic analysis, an extensive cost search was performed. During the bibliography review a great difference was observed for studies located in China in comparison to the rest of the world. Due to this, two scenarios were considered. The employed initial investment cost for the least favorable scenario was $6.0 \frac{MUSD}{MW}$ and $7.9 \frac{MUSD}{MW}$ for 110MW SPT and 55MW PT technologies respectively. In the most favorable scenario these costs fall to $5.0 \frac{MUSD}{MW}$ and $6.0 \frac{MUSD}{MW}$.

Utilizing SAM, solar field and storage sizes were optimized in five different locations, from an economic point of view, by the minimization of Levelized cost of Energy (LCOE) a widely use parameter for this kind of evaluations. As expected, Salto proved to be the most suitable location for CSP projects leading to LCOE values of $174.7 \frac{USD}{MWh}$ and $220 \frac{USD}{MWh}$ for 110 MW SPT and 55MW PT technologies respectively. This result is far from being competitive to photovoltaic ($39 \frac{USD}{MWh}$) or wind technologies ($43 \frac{USD}{MWh}$), but can be competitive against fossil fuels power plant.

A $442.5GWh$ annual electricity generation is estimated for the optimal SPT Salto study case (leading to a 45.9% capacity factor). For the optimal PT configuration considering the same location a annual electricity generation of $229.0GWh$ is estimated (47.5% capacity factor).

In addition, these results were compared to the ones presented in [18] (where no optimization is performed) showing a considerable reduction (around 10%). This shows that the solar field and storage size optimization, along with a new evaluation of the costs involved was advantageous. A sensitivity analysis was performed considering 5% variations in the initial investment and generated energy, leading to similar behaviors in the LCOE, proving these factors to be of great importance.

Moreover, the monthly produced energy for Salto optimal configuration is presented. SPT and PT study case the electricity obtained in January ascends to $65.9GWh$ and $34.4GWh$ respectively significantly higher than the $30.7GWh$ and $11.6GWh$ predicted generation for July. In order to better understand this phenomenon the importance of different losses is studied. For both technologies optical losses prevail, reaching optical efficiencies values of 49.8% and 37.8% for SPT and PT respectively. A great difference in the importance of receiver, piping and heat exchangers losses for both technologies are found, being far more significant in PT plants. An analysis of the optical efficiency is performed, leading to an important variation between summer and winter periods. When analyzing the influence of the location in the optical efficiency for the five available locations, low impact is observed.

Future works can explore the impact of considering different prices according the demand existent in the electric grid, maximizing the advantages of counting with a storage system. In addition, hybridization with fossil fuel or biomass plants can be analyzed. Finally, as the technology is still being improved cost may vary in the following years, making a new analysis necessary.

Bibliography

- [1] Islam MT, Huda N, Abdullah AB, and Saidur R. “A comprehensive review of state-of-the-art concentrating solar power (CSP) technologies: Current status and research trends”. In: *Renewable and Sustainable Energy Reviews* 91.April (2018), pages 987–1018. ISSN: 18790690. DOI: [10.1016/j.rser.2018.04.097](https://doi.org/10.1016/j.rser.2018.04.097). URL: <https://doi.org/10.1016/j.rser.2018.04.097>.
- [2] *Mercado potencial en españa y aplicaciones en tecnologías solares de concentración de media temperatura*. Technical report. Solar Concentra, 2015.
- [3] Wagner MJ and Gilman P. “Technical manual for the SAM physical trough model, by National Renewable Energy Laboratory (NREL, U.S. Department of Energy)”. In: *National Renewable Energy Laboratory* 303.June (2011), pages 275–3000. URL: <http://www.nrel.gov/docs/fy11osti/51825.pdf>.
- [4] Sun & wind energy. “*Gemasolar power tower commissioned*”. URL: <https://www.sunwindenergy.com/news/gemasolar-power-tower-commissioned>.
- [5] Wagner MJ. *Simulation and Predictive Performance Modeling of Utility-Scale Central Receiver System Power Plants* by. Technical report. National Renewable Energy Laboratory (NREL), 2008. URL: <http://sel.me.wisc.edu/publications/theses/wagner08.zip>.
- [6] Zayed ME, Zhao J, Elsheikh AH, Li W, Sadek S, and Aboelmaaref MM. “A comprehensive review on Dish/Stirling concentrated solar power systems: Design, optical and geometrical analyses, thermal performance assessment, and applications”. In: *Journal of Cleaner Production* 283 (2021), page 124664. ISSN: 09596526. DOI: [10.1016/j.jclepro.2020.124664](https://doi.org/10.1016/j.jclepro.2020.124664). URL: <https://doi.org/10.1016/j.jclepro.2020.124664>.

- [7] Wagner MJ. *Results and Comparison from the SAM Linear Fresnel Technology Performance Model*. Technical report. National Renewable Energy Laboratory (NREL), 2012.
- [8] Alonso-Suarez R. “Estimación del recurso solar en Uruguay mediante imágenes satelitales.” PhD thesis. Universidad de la República (Uruguay), 2017.
- [9] REN21. *Renewables 2019 Global Status Report*. Volume 8. 3. 2019, page 139. ISBN: 9783981891140. DOI: [10.3390/resources8030139](https://doi.org/10.3390/resources8030139).
- [10] Agency IRE. *Renewable Power Generation Costs in 2018*. 2018, page 160. ISBN: 978-92-9260-040-2. arXiv: [arXiv:1011.1669v3](https://arxiv.org/abs/1011.1669v3). URL: <https://www.irena.org/-/media/Files/IRENA/Agency/Publication/2018/Jan/IRENA%2017%202017%20Power%20Costs%202018.pdf>.
- [11] DNE. *Balance Energético Nacional*. Technical report. Dirección Nacional de Energía, 2020.
- [12] ADME. *Informe anual 2019*. Technical report. Administración del Mercado Eléctrico, 2020.
- [13] Alonso Suárez R, Bidegain M, Abal G, and Modernell P. *Año Meteorológico Típico para aplicaciones de energía solar - AMTUes Series horarias típicas para 5 sitios del Uruguay*. Technical report. Laboratorio de Energía Solar (Uruguay), 2016.
- [14] Aly A, Bernardos A, Fernandez-Peruchena CM, Jensen SS, and Pedersen AB. “Is Concentrated Solar Power (CSP) a feasible option for Sub-Saharan Africa?: Investigating the techno-economic feasibility of CSP in Tanzania”. In: *Renewable Energy* 135 (2019), pages 1224–1240. ISSN: 18790682. DOI: [10.1016/j.renene.2018.09.065](https://doi.org/10.1016/j.renene.2018.09.065). URL: <https://doi.org/10.1016/j.renene.2018.09.065>.
- [15] Praveen RP, Baseer MA, and Sankara NK. “Design. Performance Analysis and Optimization of a 100 MW Concentrated Solar Power Plant with Thermal Energy Storage”. In: *Proceedings of the 2018 International Conference on Current Trends towards Converging Technologies, ICCTCT 2018* (2018), pages 1–6. DOI: [10.1109/ICCTCT.2018.8551033](https://doi.org/10.1109/ICCTCT.2018.8551033).

- [16] Tahir S, Ahmad M, Abd-ur-Rehman HM, and Shakir S. “Techno-economic assessment of concentrated solar thermal power generation and potential barriers in its deployment in Pakistan.” In: *Journal of Cleaner Production* 293 (2021). ISSN: 09596526. DOI: [10.1016/j.jclepro.2021.126125](https://doi.org/10.1016/j.jclepro.2021.126125).
- [17] Dos Santos MP, Leite LH, and Da Silva Reis A. “Concentrated solar power: Analysis of economic aspects in Brazil”. In: *2017 IEEE PES Innovative Smart Grid Technologies Conference - Latin America, ISGT Latin America 2017* 2017-Janua (2017), pages 1–6. DOI: [10.1109/ISGT-LA.2017.8126691](https://doi.org/10.1109/ISGT-LA.2017.8126691).
- [18] *Análisis de pre-factibilidad para el desarrollo de energía termosolar en Uruguay*. Technical report. Solida renewable energies, 2014.
- [19] Ho CK. *Software and Codes for Analysis of Concentrating Solar Power Technologies*. Technical report. Sandia National Laboratories, 2008.
- [20] John W. Eaton. “GNU Octave”. URL: <https://www.gnu.org/software/octave/index>.
- [21] Duffie JA and Beckman WA. *Solar engineering of thermal processes*. John Wiley and sons, INC, 2006.
- [22] Forristall R. *Heat Transfer Analysis and Modeling of a Parabolic Trough Solar Receiver Implemented in Engineering Equation Solver*. Technical report. National Renewable Energy Laboratory (NREL), 2003.
- [23] Montes MJ, Abánades A, Martínez-Val JM, and Valdés M. “Solar multiple optimization for a solar-only thermal power plant, using oil as heat transfer fluid in the parabolic trough collectors”. In: *Solar Energy* 83.12 (2009), pages 2165–2176. ISSN: 0038092X. DOI: [10.1016/j.solener.2009.08.010](https://doi.org/10.1016/j.solener.2009.08.010).
- [24] Incropera F, Dewitt D, Bergman T, and Lavine A. *Heat and mass transfer*. John Wiley and sons, INC, 2017.
- [25] National Renewable Energy Laboratory. “System Advisor Model”. URL: <https://sam.nrel.gov/>.
- [26] Blair N et al. “System Advisor Model (SAM) General Description System Advisor Model (SAM) General Description (Version 2017 . 9 . 5)”. In: May (2018).

- [27] Investopedia. "<https://www.investopedia.com/>". URL: <https://www.investopedia.com/>.
- [28] Economía y Finanzas M de. *Decreto 143/018*. URL: <https://www.impo.com.uy/bases/decretos/143-2018>.
- [29] Solutia. *Therminol VP-1*.
- [30] IRENA. *Renewable Power Generation Costs in 2019*. Technical report. International Renewable Energy Agency, 2020.
- [31] Economía y Finanzas M de. *Simulador del sector industria*. URL: https://www.mef.gub.uy/25022/7/areas/simuladores-dec-143%7B%5C_%7D018.html.
- [32] DensityDesign, Calibro and Inmagik. "*RAWGraphs*". URL: <https://app.rawgraphs.io/>.
- [33] Andrew Marsh. "*3D Sun Path*". URL: <https://drajmarsh.bitbucket.io/sunpath3d.html>.
- [34] Yang S, Zhu X, and Guo W. "Cost-Benefit Analysis for the Concentrated Solar Power in China". In: *Journal of Electrical and Computer Engineering* 2018 (2018). ISSN: 20900155. DOI: [10.1155/2018/4063691](https://doi.org/10.1155/2018/4063691).
- [35] Ling-zhi R, Xin-gang Z, Yu-zhuo Z, and Yan-bin L. "The economic performance of concentrated solar power industry in China". In: *Journal of Cleaner Production* 205 (2018), pages 799–813. ISSN: 09596526. DOI: [10.1016/j.jclepro.2018.09.110](https://doi.org/10.1016/j.jclepro.2018.09.110). URL: <https://doi.org/10.1016/j.jclepro.2018.09.110>.
- [36] Nadav Shemer. "*CSP capex costs fall by almost half as developers shift towards China and Middle East*". URL: <https://www.reutersevents.com/renewables/csp-today/csp-capex-costs-fall-almost-half-developers-shift-towards-china-and-middle-east>.
- [37] Simsek Y, Mata-torres C, Escobar R, and Cardemil JM. "Incentives and financial conditions effect analysis on levelized cost of electricity (LCOE) and government cost for concentrated solar power (CSP) projects in Chile". In: 160004.2017 (2018).

- [38] Santos JJ, Palacio JC, Reyes AM, Carvalho M, Freire AJ, and Barone MA. “Concentrating Solar Power”. In: *Advances in Renewable Energies and Power Technologies* 1.2 (2018), pages 373–402. DOI: [10.1016/B978-0-12-812959-3.00012-5](https://doi.org/10.1016/B978-0-12-812959-3.00012-5).
- [39] *Development of Local Supply Chain : The Missing Link for Concentrated Solar Power Projects in India*. Technical report. Energy sector management assistance program, 2013.
- [40] Boretti A. “Cost and production of solar thermal and solar photovoltaics power plants in the United States”. In: *Renewable Energy Focus* 26.00 (2018), pages 93–99. ISSN: 17550084. DOI: [10.1016/j.ref.2018.07.002](https://doi.org/10.1016/j.ref.2018.07.002). URL: <https://doi.org/10.1016/j.ref.2018.07.002>.

APPENDICES

Appendix A

Results

The solar field and storage optimization for each technology and location is presented in this chapter. Moreover, the main results obtained for these cases including gross solar energy, incident energy on the absorber (discounting optical losses), net generated energy and total plant efficiency. For PT technologies, two different incident gross solar energy values are presented leading to two values for optical efficiency and total efficiency. The first value calculates the incident gross solar energy as the product of irradiance and reflective area while the second also takes into account cosine losses.

A.1 Location: Salto

A.1.1 Optimal configuration

Table A.1: Solar Power Tower optimal configuration Salto.

Heliostat number	Storage size (h)					
	5.0	7.5	10	12.5	15	17.5
16770	198.7	-	-	-	-	-
18295	-	187.8	183.5	184.0	-	-
20223	-	187.5	180.8	179.3	-	-
21780	-	-	180.5	177.5	179	-
23335	-	-	180	174.7	175.2	-
24891	-	-	-	174.7	174.4	
26447	-	-	-	175.1	174.4	175.5

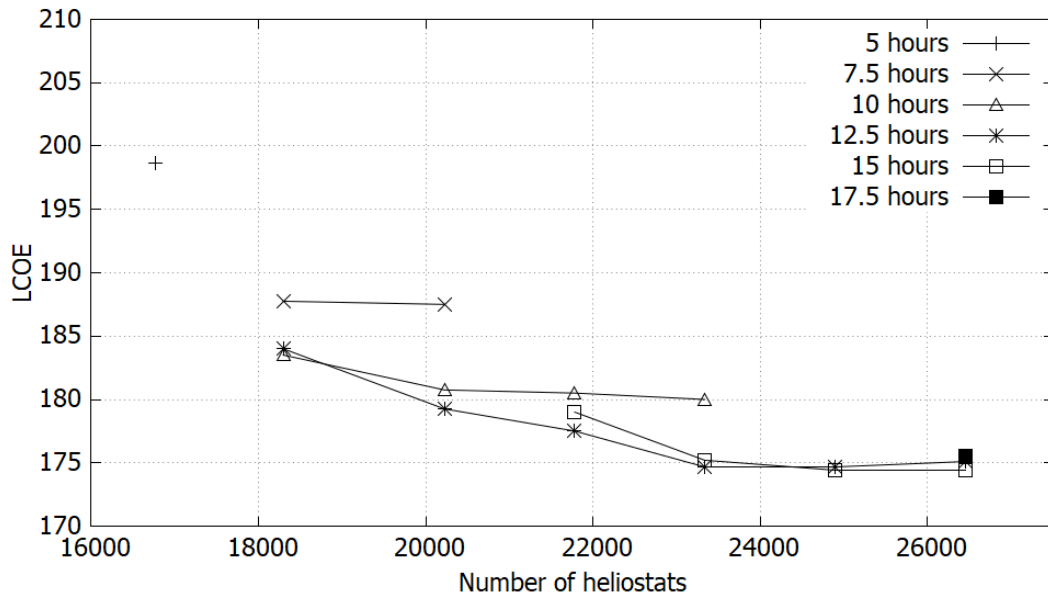


Figure A.1: LCOE optimization Power Tower Salto study case.

Table A.2: Parabolic Trough optimal configuration Salto.

N° loops	Storage size (h)						
	0	5	7.5	10	12.5	15	17.5
92	242.0	-	-	-	-	-	-
126	245.0	235.0	249.0	-	-	-	-
190	-	231.8	223.5	225.0	-	-	-
222	-	-	225.0	221.5	221.5	225.5	-
254	-	-	-	223.0	220.2	219.7	-
286	-	-	-	-	221.1	219.7	225.8

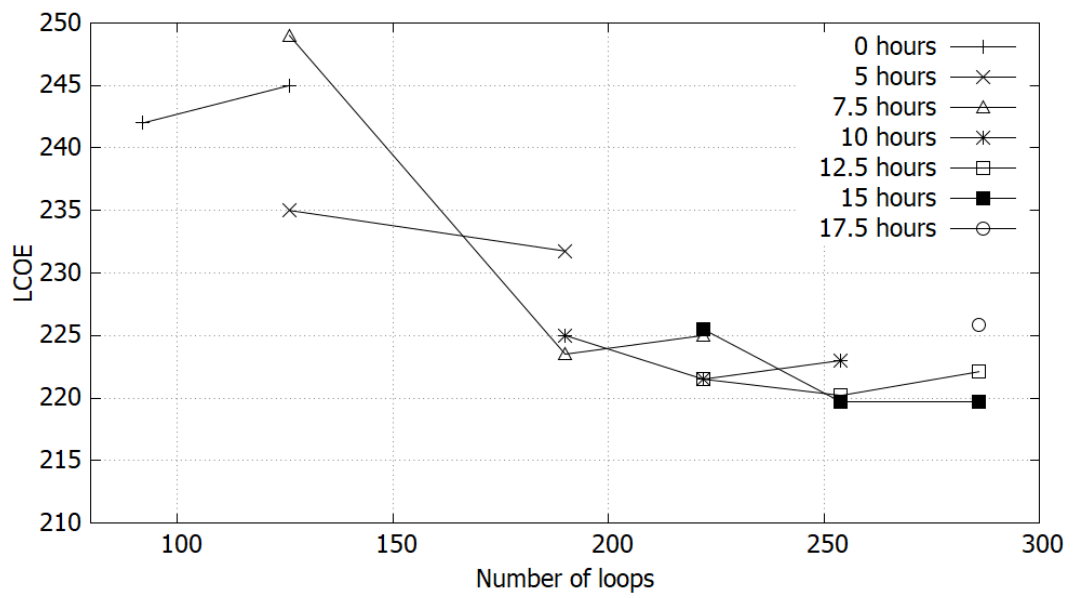


Figure A.2: LCOE optimization Parabolic Trough Salto study case.

A.1.2 Energy simulation

Table A.3: Main results for optimal SPT plant located in Salto.

Gross power output	110 MW
Storage	12.5 hours
Number of heliostats	23335
DNI	$1897.5 \frac{kWh}{m^2 \cdot year}$
Heliostat area	$66.1 m^2$
Heliostat reflectivity	0.935
Cleanliness factor	0.98
Hot HTF temperature	565.8 ° C
Cold HTF temperature	287.8 ° C
Gross solar energy	2926.8 GWh
Receptor incident energy	1358.9 GWh
Optical efficiency	46.4%
Energy transferred to HTF	1160 GWht
Cycle efficiency	47.0%
Net energy generated	442.5 GWhe
Total efficiency	15.1%

Table A.4: Main results for optimal PT plant located in Salto.

Gross power output	55 MW
Storage	12.5 hours
Number of loops	254
DNI	$1897.5 \frac{kWh}{m^2 \cdot year}$
Loop area	$3462 m^2$
Heliostat reflectivity	0.935
Cleanliness factor	0.97
Absorptivity	0.96
Transmissivity	0.96
Hot HTF temperature	393.0 ° C
Cold HTF temperature	293.0 ° C
Gross solar energy	1668.6 GWht - 1501.5 GWht
Receptor incident energy	1033.8 GWht
Optical efficiency	62.05 % - 68.9 %
Energy transferred to HTF	700.0 GWht
Cycle efficiency	37.3 %
Net energy generated	229.0 GWhe
Total efficiency	13.7 % - 15.3 %

A.2 Location: Colonia

A.2.1 Optimal configuration

Table A.5: Solar Power Tower optimal configuration Colonia.

Number of heliostats	Storage size (h)			
	10	12.5	15	17.5
21780	180.8	178.4	181.1	-
23335	180.3	176.4	177.5	-
24891	181.3	176.0	176.4	
26447	-	176.3	176.0	177.7

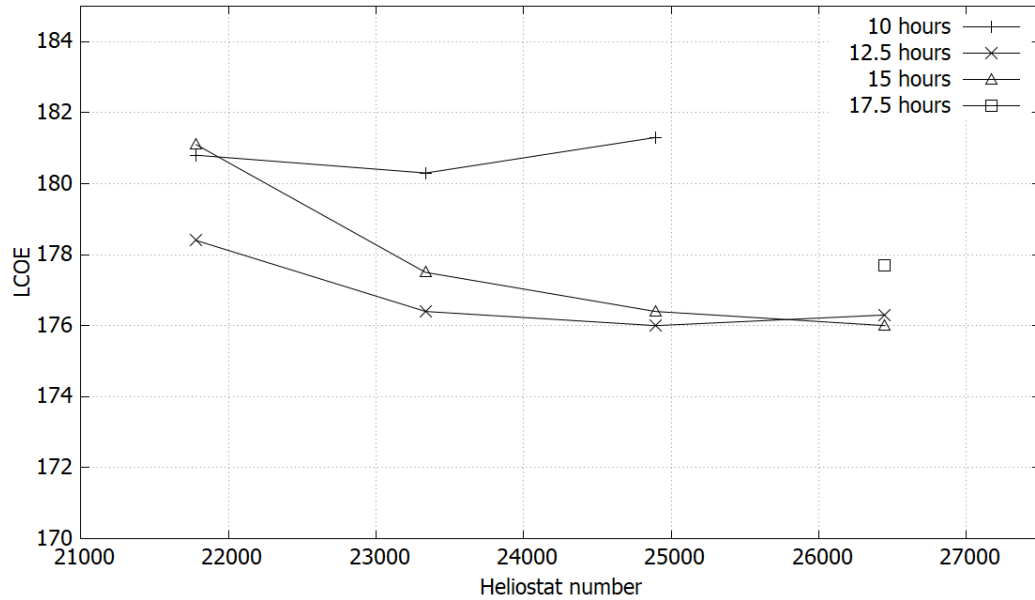


Figure A.3: LCOE optimization Power Tower Colonia study case.

Table A.6: Parabolic Trough optimal configuration Colonia.

N° loops	Storage size (h)		
	10	12.5	15
222	223.0	224.1	-
254	222.6	220.9	223.1
286	225.9	221.5	221.9
318	-	-	221.8

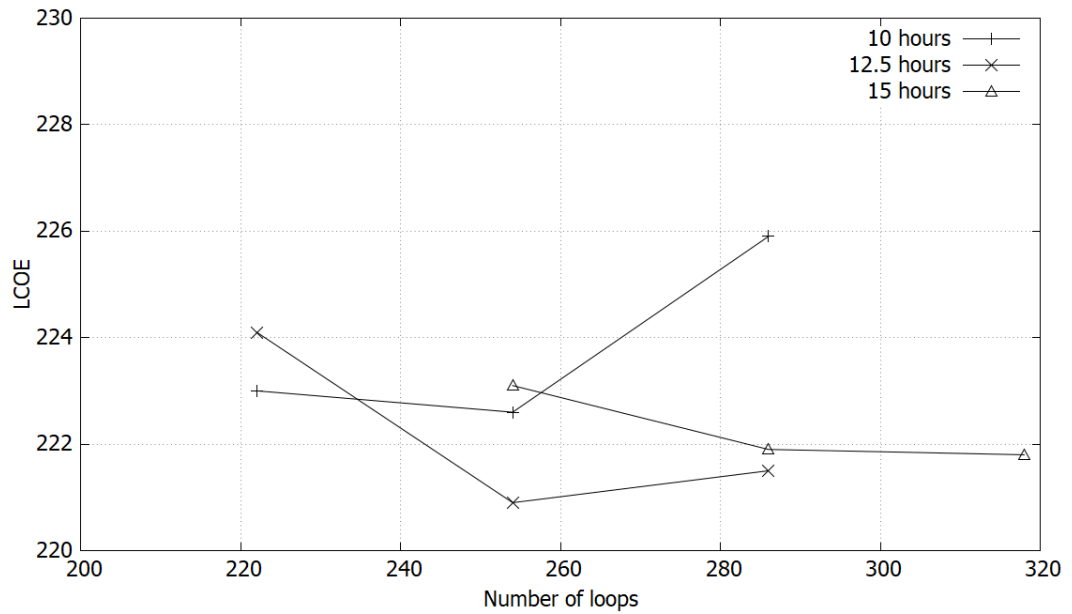


Figure A.4: LCOE optimization Parabolic Trough Colonia study case.

A.2.2 Energy simulation

Table A.7: Main results for optimal SPT plant located in Colonia.

Gross power output	110 MW
Storage	12.5 hours
Number of heliostats	24891
DNI	$1890.3 \frac{kWh}{m^2 \cdot year}$
Heliostat area	$66.1 m^2$
Heliostat reflectivity	0.935
Cleanliness factor	0.98
Hot HTF temperature	565.8 ° C
Cold HTF temperature	287.8 ° C
Gross solar energy	3110 GWh
Receptor incident energy	1393.3 GWh
Optical efficiency	44.8%
Energy transferred to HTF	1176.4 GWht
Cycle efficiency	47.1%
Net energy generated	450.8 GWhe
Total efficiency	14.5%

Table A.8: Main results for optimal PT plant located in Colonia.

Gross power output	55 MW
Storage	12.5 hours
Number of loops	254
DNI	$1890.3 \frac{kWh}{m^2 \cdot year}$
Loop area	$3462 m^2$
Heliostat reflectivity	0.935
Cleanliness factor	0.97
Absorptivity	0.96
Transmissivity	0.96
Hot HTF temperature	393.0 ° C
Cold HTF temperature	293.0 ° C
Gross solar energy	1662.2 GWht - 1464.6 GWht
Receptor incident energy	1001.4 GWht
Optical efficiency	60.2 % - 68.4 %
Energy transferred to HTF	688.4 GWht
Cycle efficiency	37.6 %
Net energy generated	227.8 GWhe
Total efficiency	13.7 % - 15.6 %

A.3 Location: Montevideo

A.3.1 Optimal configuration

Table A.9: Solar Power Tower optimal configuration Montevideo.

Number of heliostats	Storage size (h)		
	10	12.5	15
21780	187.1	183.0	185.3
23335	186.9	181.8	182.6
24891	188.1	182.2	182.2
26447	-	-	182.1

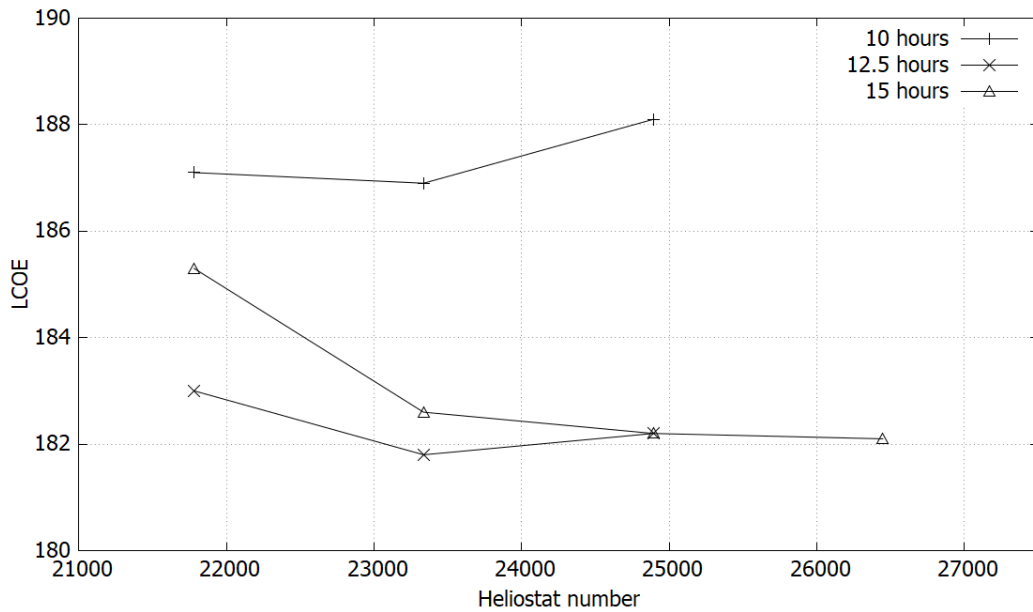


Figure A.5: LCOE optimization Power Tower Montevideo study case.

Table A.10: Parabolic Trough optimal configuration Montevideo.

N° loops	Storage size (h)		
	10	12.5	15
222	229.6	229.7	-
254	230.4	227.3	229.3
286	-	229.6	229.9

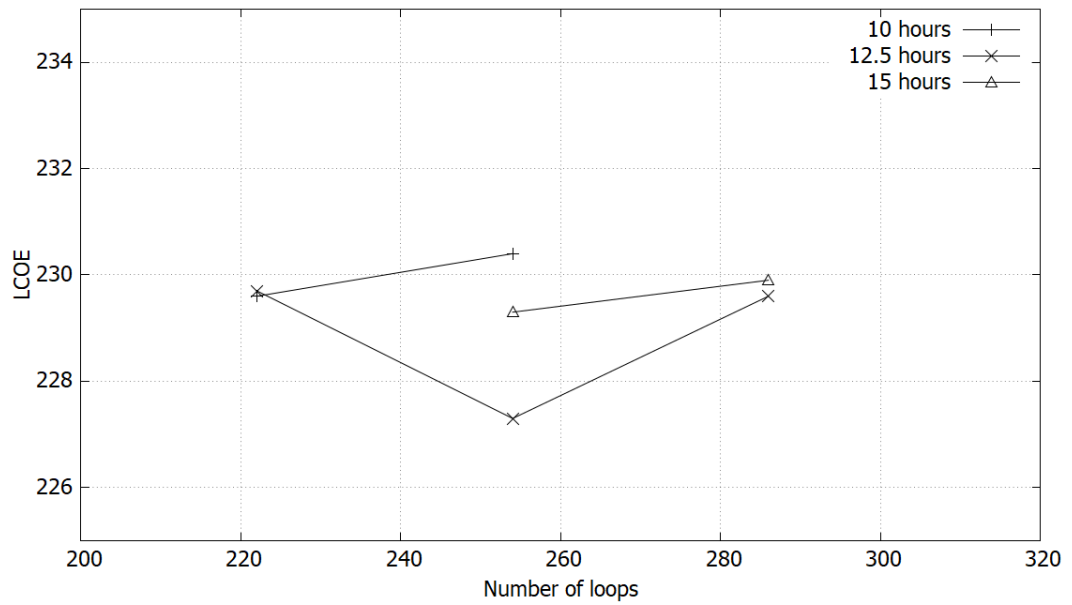


Figure A.6: LCOE optimization Parabolic Trough Montevideo study case.

A.3.2 Energy simulation

Table A.11: Main results for optimal SPT plant located in Montevideo.

Gross power output	110 MW
Storage	12.5 hours
Number of heliostats	23335
DNI	$1862.5 \frac{kWh}{m^2 \cdot year}$
Heliostat area	$66.1 m^2$
Heliostat reflectivity	0.935
Cleanliness factor	0.98
Hot HTF temperature	565.8 ° C
Cold HTF temperature	287.8 ° C
Gross solar energy	2872.3 GWh
Receptor incident energy	1311.6 GWh
Optical efficiency	45.7%
Energy transferred to HTF	1106.2 GWht
Cycle efficiency	47.2%
Net energy generated	425.2 GWhe
Total efficiency	14.8%

Table A.12: Main results for optimal PT plant located in Montevideo

Gross power output	55 MW
Storage	12.5 hours
Number of loops	254
DNI	$1862.5 \frac{kWh}{m^2 \cdot year}$
Loop area	$3462 m^2$
Heliostat reflectivity	0.935
Cleanliness factor	0.97
Absorptivity	0.96
Transmisivity	0.96
Hot HTF temperature	393.0 ° C
Cold HTF temperature	293.0 ° C
Gross solar energy	1637.8 GWht - 1463.7 GWht
Receptor incident energy	1000.0 GWht
Optical efficiency	61.0 % - 68.3 %
Energy transferred to HTF	669.3 GWht
Cycle efficiency	37.8 %
Net energy generated	221.7 GWhe
Total efficiency	13.5 % - 15.1 %

A.4 Location: Rivera

A.4.1 Optimal configuration

Table A.13: Solar Power Tower optimal configuration Rivera.

Number of heliostats	Storage size (h)		
	10	12.5	15
21780	189.9	187.0	189.7
23335	189.7	184.8	185.5
24891	191.2	184.7	184.3
26447	-	-	184.0

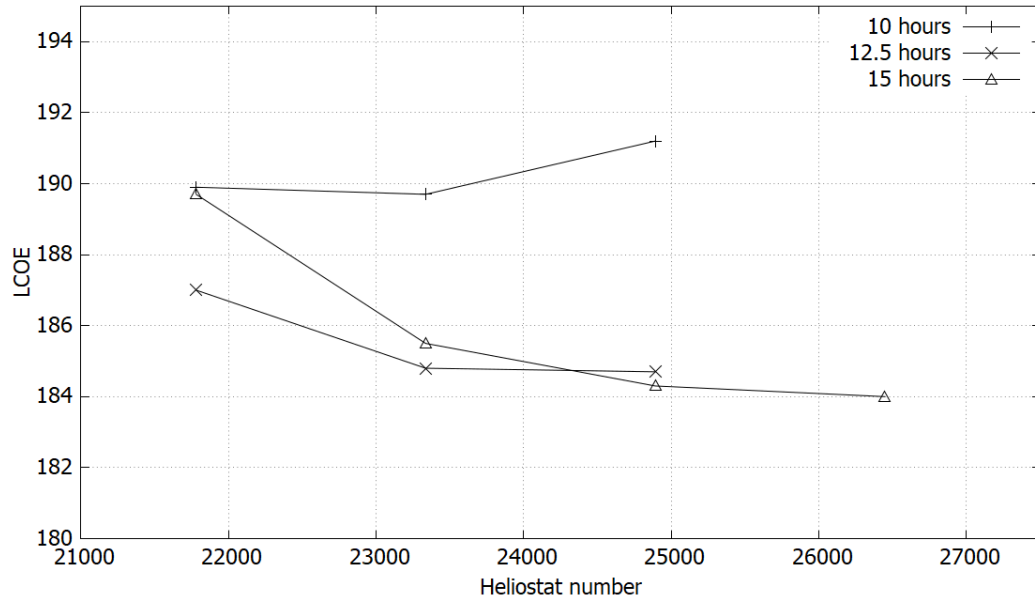


Figure A.7: LCOE optimization Solar Power Tower Rivera study case.

Table A.14: Parabolic Trough optimal configuration Rivera.

N° loops	Storage size (h)		
	10	12.5	15
222	238.7	240.0	-
254	246.6	236.7	237.1
286	-	239.1	236.1
318	-	-	237.8

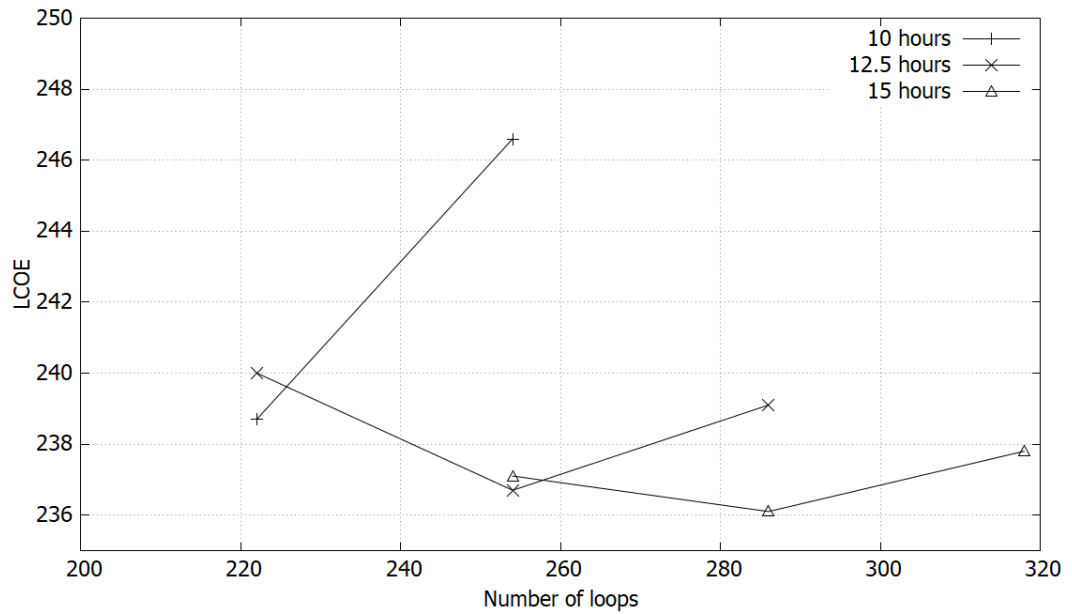


Figure A.8: LCOE optimization Parabolic Trough Rivera study case.

A.4.2 Energy simulation

Table A.15: Main results for optimal SPT plant located in Rivera.

Gross power output	110 MW
Storage	15 hours
Number of heliostats	24891
DNI	$1779.7 \frac{kWh}{m^2 \cdot year}$
Heliostat area	$66.1 m^2$
Heliostat reflectivity	0.935
Cleanliness factor	0.98
Hot HTF temperature	565.8 ° C
Cold HTF temperature	287.8 ° C
Gross solar energy	2745.1 GWh
Receptor incident energy	1261.5 GWh
Optical efficiency	46.0%
Energy transferred to HTF	1150.0 GWht
Cycle efficiency	47.1%
Net energy generated	439.5 GWhe
Total efficiency	16.0%

Table A.16: Main results for optimal PT plant located in Rivera.

Gross power output	55 MW
Storage	15 hours
Number of loops	286
DNI	$1779.7 \frac{kWh}{m^2 \cdot year}$
Loop area	$3462 m^2$
Heliostat reflectivity	0.935
Cleanliness factor	0.97
Absorptivity	0.96
Transmissivity	0.96
Hot HTF temperature	393.0 ° C
Cold HTF temperature	293.0 ° C
Gross solar energy	1565.0 GWht - 1380.0 GWht
Receptor incident energy	937.9 GWht
Optical efficiency	60.0 % - 68.0 %
Energy transferred to HTF	718.2 GWht
Cycle efficiency	37.8 %
Net energy generated	238.4 GWhe
Total efficiency	15.2 % - 17.3 %

A.5 Location: Rocha

A.5.1 Optimal configuration

Table A.17: Solar Power Tower optimal configuration Rocha.

Number of heliostats	Storage size (h)		
	10	12.5	15
21780	200.4	197.7	200.0
23335	200.2	195.5	195.8
24891	201.3	195.0	194.7
26447	-	195.7	194.5

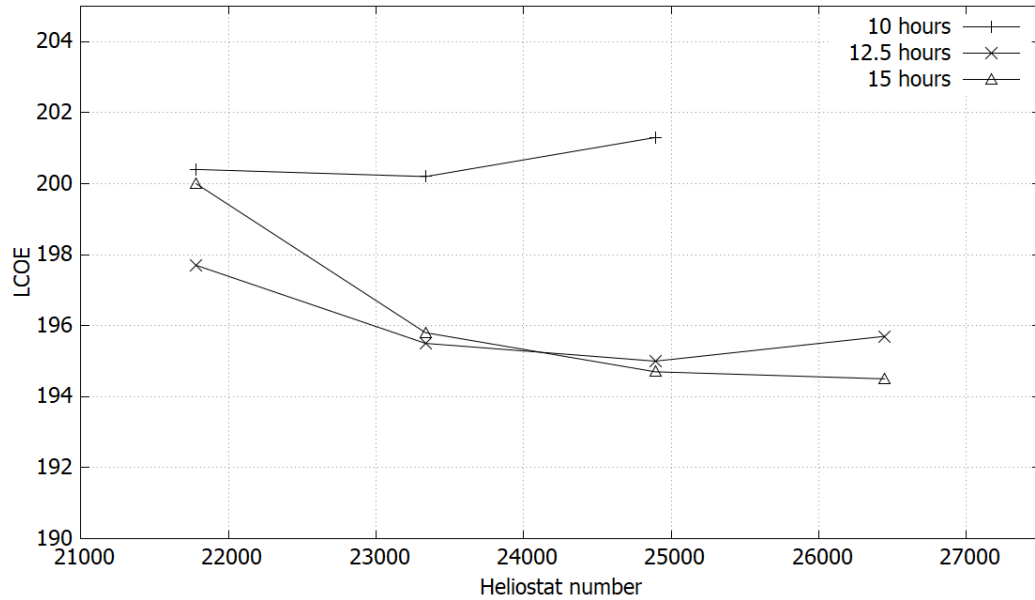


Figure A.9: LCOE optimization Solar Power Tower Rocha study case.

Table A.18: Parabolic Trough optimal configuration Rocha.

N° loops	Storage size (h)		
	10	12.5	15
222	246.0	247.0	-
254	246.6	243.7	245.2
286	-	246.0	244.3
318	-	-	245.5

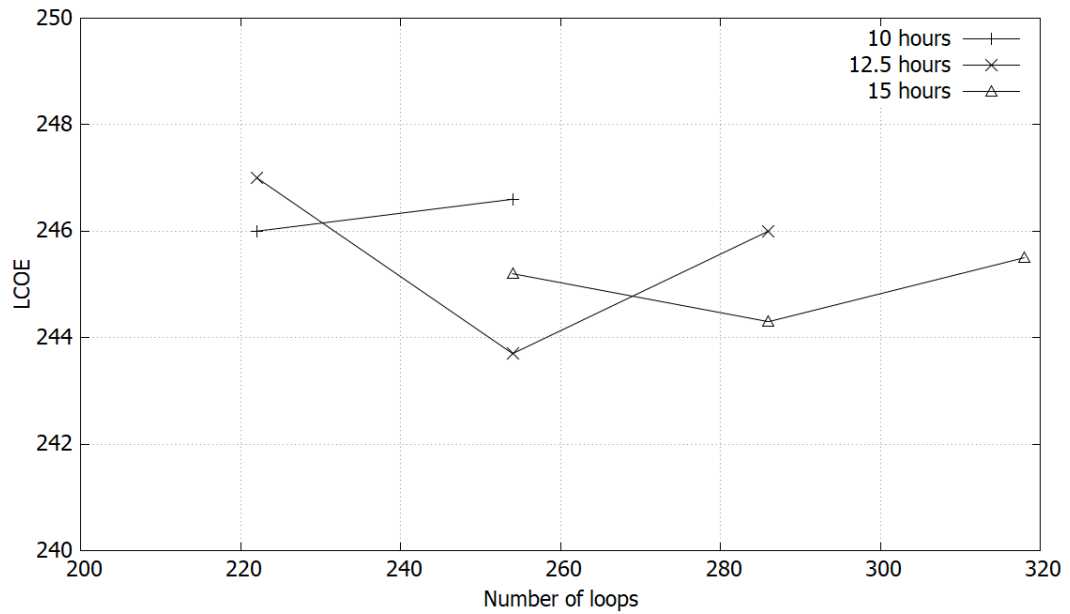


Figure A.10: LCOE optimization Parabolic Trough Rocha study case.

A.5.2 Energy simulation

Table A.19: Main results for optimal SPT plant located in Rocha.

Gross power output	110 MW
Storage	15 hours
Number of heliostats	24891
DNI	$1740.6 \frac{kWh}{m^2 \cdot year}$
Heliostat area	$66.1 m^2$
Heliostat reflectivity	0.935
Cleanliness factor	0.98
Hot HTF temperature	565.8 ° C
Cold HTF temperature	287.8 ° C
Gross solar energy	2684.8 GWh
Receptor incident energy	1210.6 GWh
Optical efficiency	45.0%
Energy transferred to HTF	1083.7 GWht
Cycle efficiency	47.2%
Net energy generated	415.7 GWhe
Total efficiency	15.5%

Table A.20: Main results for optimal PT plant located in Rocha.

Gross power output	55 MW
Storage	12.5 hours
Number of loops	254
DNI	$1740.6 \frac{kWh}{m^2 \cdot year}$
Loop area	$3462 m^2$
Heliostat reflectivity	0.935
Cleanliness factor	0.97
Absorptivity	0.96
Transmissivity	0.96
Hot HTF temperature	393.0 ° C
Cold HTF temperature	293.0 ° C
Gross solar energy	1530.6 GWht - 1357.7 GWht
Receptor incident energy	915.4 GWht
Optical efficiency	59.8 % - 67.4 %
Energy transferred to HTF	652.2 GWht
Cycle efficiency	37.7 %
Net energy generated	206.1 GWhe
Total efficiency	13.5 % - 15.2 %

Appendix B

Cost estimation

A key aspect for performing a good analysis is to accurately determine the cost involved in the development of these projects. An extensive literature review was performed, leading to different initial investment costs which are presented in Tables B.1 to B.6 discriminated by installed capacity and technology. Tables B.1 to B.3 show information of SPT technologies of 55MW, 110 MW and unknown installed capacity respectively. Tables B.4 to B.6 present the same information for PT technology. Other relevant aspects such as the project location, available irradiation in the considered zone and storage size are also specified.

Table B.1: Solar Power Tower 50 MW initial investment(I.I.) costs.

Solar Power Tower				
I.I. (MUSD/MW)	DNI (kWh/year)	Storage (hours)	Country	Reference
50 MW				
5.1	1800	9	China	[34]
3.0-3.5	1976	6	China	[34]-[35]
3.5	1900	6	China	[34]
4.5-5.29	1870	8	China	[34]-[35]
3.9	1870	6	China	[36]
5.0	1869	8	China	[36]
6.0	1800	9	China	[35]
5.3	1600	12	China	[35]

Table B.2: Solar Power Tower 100 MW initial investment (I.I.) costs.

Solar Power Tower				
I.I. (MUSD/MW)	DNI (kWh/year)	Storage (hours)	Country	Reference
100 MW				
4.3	1800	10	China	[34]
4.4	2000	11	China	[34]
3.6	1900	8	China	[34]
4.0	1633	8	China	[36]
4.9	1633	11	China	[36]
5.1	2000	11	China	[35]
4.2	1900	8	China	[35]
5.0	1800	10	China	[35]
9.2	-	14	Chile	[37]
6.7	-	10	Salto	[18]

Table B.3: Solar Power Tower unknown capacity initial investment (I.I.) costs.

Solar Power Tower		
I.I. (MUSD/MW)	Storage (hours)	Reference
Unknown capacity and location		
7.3	7.5	[38]
6.3	6	[38]
7.4	9	[38]
7.5	6	[38]
7.7	9	[38]
9.0	12	[38]
10.5	15	[38]

Table B.4: Parabolic Trough 50MW initial investment (I.I.) cost.

Parabolic Trough				
I.I. (MUSD/MW)	DNI (kWh/year)	Storage (hours)	Country	Reference
50 MW				
5.7	2057	11	China	[34]
4.3	1800	9	China	[36]
6.2	1904	9	China	[36]
6.4	1733	15	China	[36]
4.5	1878	9	China	[35]
6.5	1976	9	China	[35]
9.0	-	6	India	[39]
5.8	-	0	India	[39]
6.1	-	7.5	Salto	[18]

Table B.5: Parabolic Trough 100MW initial investment (I.I.) cost.

Parabolic Trough				
I.I. (MUSD/MW)	DNI (kWh/year)	Storage (hours)	Country	Reference
100 MW				
4.5	1851	10	China	[36]
4.7	2025	10	China	[35]
7.9	-	14	Chile	[37]

Table B.6: Parabolic Trough unknown capacity initial investment (I.I.) costs.

Parabolic Trough		
I.I. (MUSD/MW)	Storage (hours)	Reference
Unknown capacity and location		
4.6	No	[38]
7.1	No	[38]
8.0	6.0	[38]
9.0	6.3	[38]
7.7	6	[38]
7.4	4.5	[38]
7.6	9	[38]
9.1	13.4	[38]

Table B.7: USA CSP power plants initial investment [40]

	Start of production	Technology	Storage	Nameplate Capacity MW	I.I. (MUSD/MW)
ISEGS	Jan-14	ST	No	377	6.084
Solana	Oct-13	PT	Yes	250	8.258
Genesis	Mar-14	PT	No	250	5.213
Mojave Solar Project	Dec-14	PT	No	250	6.672
Crescent Dunes	Nov-15	ST	Yes	110	9.227

Table B.8: Spain CSP power plants initial investment. Source:<https://solarpaces.nrel.gov/by-country/ES>

	Start of production	Technology	Storage	Nameplate capacity MW	I.I. (M €/MW)
Andasol 3	Aug-11	PT	7.5	50	6.3
Arcosol 50	Dec-11	PT	7.5	50	5.4
Borges Termosolar	Dec-12	PT	7.5	22.5	6.8
Gemasolar	Apr-11	SPT	15	20	11.5
Ibersol	09	PT	No	50	6.3
La Africana	Nov-12	PT	7.5	50	7.7
Moron	May-12	PT	No	50	5.9
Olivenza	Sep-12	PT	No	50	5.7
Orellana	Aug-12	PT	No	50	4.8

Table B.9: Specific investment costs Solar Power Tower [25].

Solar Power Tower	
Land improvement	16 (<i>USD/m²</i>)
Tower fixed cost	3E6 (USD)
Tower factor	0.0113
Reference receiver cost	103.6E6(USD)
Reference receiver Area	1571m ²
Receiver factor	0.7
Solar Field	145 (<i>USD/m²</i>)
Storage	24(USD/MWht)
Power plant	1100 (USD/kW)
BOP	340(USD/kW)
Land	10000 (USD/acre)
Fixed O&M	66(USD/kW-año)
Variable O&M	3.5(USD/MWh)
CAPEX (MUSD)	658.3
OPEX(MUSD/year)	8.9
I.I. (MUSD/MW)	6.0

Table B.10: Specific investment costs Parabolic Trough [25].

Parabolic Trough	
Land improvement	25 (<i>USD/m²</i>)
Solar Field	150 (<i>USD/m²</i>)
HTF system	60 (USD/m ²)
Storage	65(USD/MWht)
Power plant	1150 (USD/kW)
BOP	120(USD/kW)
Land	10000 (USD/acre)
Fixed O&M	66(USD/kW-año)
Variable O&M	4(USD/MWh)
CAPEX (MUSD)	433.8
OPEX(MUSD/year)	4.5
I.I. (MUSD/MW)	7.9

Where BOP is the balance of plant that represent the auxiliary systems of a power plant, *O&M* stands for operation and maintainance costs, CAPEX the companies long term expenses (such as machinery and equipment) and OPEX are day to day expenses such as salaries.